



# Study on narrow gap welding of martensitic grade P92 and austenitic grade AISI 304L SS steel for ultra-supercritical power plant application

Gaurav Dak<sup>1</sup> · Navneet khanna<sup>2</sup> · Chandan Pandey<sup>1</sup>

Received: 25 May 2022 / Revised: 8 September 2022 / Accepted: 1 October 2022 / Published online: 26 October 2022  
© Wrocław University of Science and Technology 2022

## Abstract

The present work investigated the microstructural feature, mechanical properties, and residual stress variation for the dissimilar welded joints (DWJs) of P92 and AISI 304L steel. The multi-pass DWJs were attempted for narrow gap geometry using the tungsten inert gas (TIG) welding process employing the ERNiCrMo-3 filler metal. The martensitic microstructure produced in the P92 HAZ region after welding is brittle due to quenched martensite and the dissolution of precipitates. Thus, the post-weld heat treatment (PWHT) known as tempering was carried out at 760 °C for a period of 2 h to get tempered martensitic microstructure and re-precipitation of dissolved precipitates. The radiographic examination and macrostructure analysis showed defect-free P92/304L SS DWJs. The weld metal showed the complete austenitic microstructure with a Ni weight percentage of 36%. However, segregation of the alloying elements along with the inter-dendritic areas and variation in grain growth during solidification was observed. There is columnar grain morphology at interface, cellular, and equiaxed in the center. The major segregation along the inter-dendritic areas was observed for Nb, Mo, Ti, and Cr that led to the formation of the carbides of type Mo<sub>6</sub>C, TiC, and NbC, which was confirmed from the energy dispersive spectroscopy (EDS) analysis. From the tensile test result, 304L SS base metal (BM) was inferred as the weakest region in P92/304L SS DWJs. The ultimate tensile strength (UTS) of the as-weld joint was about 626 MPa, along with fracture location in 304L SS base metal. The Charpy impact test results showed that the region with relatively poor impact toughness was austenitic ERNiCrMo-3 filler weld (57 J) which might be due to the segregation of the Nb and Mo along the inter-dendritic areas. However, the impact toughness of the ERNiCrMo-3 filler weld met the minimum requirement of 47J (EN ISO 3580:2017). The micro-hardness result showed that in the as-welded condition, the coarse grain heat affected zone (CGHAZ) has the highest micro-hardness value (340 HV) due to the high weight percentage of Cr and N resulting from the dissolution of M<sub>23</sub>C<sub>6</sub> precipitates followed by the fine grain heat affected zone (FGHAZ, 270 HV), and the inter-critical heat affected zone (ICHAZ, 205 HV). After PWHT, the hardness value was decreased below the maximum allowable value of 265 HV due to the tempering of the martensite. The residual stresses developed in the case of the narrow groove design were less due to the less quantity of weld metal available for volumetric contraction in the case of the narrow groove geometry. The tensile stress was dominant in the weld fusion zone due to the volumetric contraction of the weld metal, while compressive stress was dominant in P92 HAZ because of the martensitic phase transformation.

**Keywords** Narrow gap welding · ERNiCrMo-3 filler · Interface · Characterization · Residual stress

## 1 Introduction

Worldwide, coal plays a vital role in electricity generation, and about 40% of the world's electricity is produced from coal-fired power plants (CFPPs) [1]. The relatively low cost and wide availability of coal compared to oil and natural gas has been a leading source of power generation for many decades [2]. However, the emission of many pollutants from coal-fired power plants makes coal the largest single source of CO<sub>2</sub> emission, which affects the overall quality of the air.

✉ Chandan Pandey  
jscpandey@iitj.ac.in; chandanpy.1989@gmail.com

<sup>1</sup> Department of Mechanical Engineering, Indian Institute of Technology (IIT) Jodhpur, Karwar, Rajasthan 342037, India

<sup>2</sup> Advanced Manufacturing Laboratory, Institute of Infrastructure Technology Research and Management, Ahmedabad 380026, India

Control of CO<sub>2</sub> emission is a key task for the government looking for a way to have a low or zero-emission energy system. The increase in efficiency of the existing plants and development of the new plants with higher efficiency anywhere in the world is a path of no regret as efficient plants help to minimize CO<sub>2</sub> emissions by reducing fuel consumption. In their study, Campbell et al. [2] reported that an increase in the efficiency of the existing power plants could result in a drastic reduction in CO<sub>2</sub> emission. The major component in greenhouse gas emissions from CFPPs is CO<sub>2</sub>; hence, reducing CO<sub>2</sub> by improving the efficiency of existing plants is directly related to reducing greenhouse gas emissions. The sub-critical power plants are designed to operate at a temperature of about 540 °C and could achieve maximum efficiency of 40%, while for super-critical plants having an operating temperature of about 600–615 °C, efficiency could achieve about 42%. The increase in efficiency by 2% reduces CO<sub>2</sub> emissions by 4% [3]. The advanced ultra-supercritical CFPPs are designed to operate at a temperature of more than 700 °C with an efficiency of 46–48%, and it reduces the CO<sub>2</sub> emission by 18–22% per MWh of electricity produced as compared to equivalent size sub-critical CFPPs. However, due to the involvement of novel materials, i.e., high cost, the major up-gradation of existing CFPPs has involved the conversion of subcritical and supercritical CFPPs to ultra super-critical (USC) CFPPs. The increase in efficiency of CFPPs is achieved by increasing the temperature of the working steam at the turbine inlet [4]. Alvin et al. [5] reported that an increase in steam temperature by 10 °C increases the net efficiency by 0.5%. The USC plants are now considered state of the art and can operate up to the temperature of 650 °C with efficiency in the range of 42–46%.

The increase in operating temperature of steam results in a tremendous need for heat-resistant novel material in USC plants, and it paved the way for the development of many alloys, and new generation creep strength enhanced ferritic/martensitic (CSEF) steels like P91, P92, SS304L, and SS304H steel [6]. Nippon Steel Corporation developed martensitic grade P92 steel in the late 1990s for heavy section tubular components by altering the composition of P91 steel. The austenitic stainless steel (ASS) is a less expansive material and owns good corrosion resistance, excellent mechanical property, and is less prone to sensitization. It has good weldability because of its low carbon content. The steam header made of P92 is connected with the boiler reheater and superheater tube made of 304L SS. Thus, the joining of P92 steel and 304L SS becomes essential. However, this is not an easy task due to the difference in chemical composition and physical and mechanical properties of these two materials [7]. The problems most commonly associated with the joining of martensitic and austenitic stainless steel are carbon migration from ferritic to austenitic steel

(from the low chromium side to the high chromium side), solidification cracking, heterogeneous microstructure development, and high residual stress at the weld interface due to the mismatch in co-efficient of thermal expansion between dissimilar metals. The carbon migration leads to the formation of the carbon-depleted zone (CDZ) and carbon-enriched zone (CEZ) near the weld interface. The formation of CDZ and CEZ are undesirable as they reduce the creep strength of the DWJs due to the formation of detrimental laves phases in these regions after long-term service at elevated temperature [8]. Austenitic filler metals are not suitable for joining martensitic and austenitic steel due to their poor performance at elevated temperatures. Also, austenitic filler metals are prone to solidification cracking and premature creep failure. The nickel-based filler metal can solve many of the above-listed issues. The nickel-based filler is frequently used to join different grades of steel, such as joining low alloy steel or carbon steel with stainless steel. The martensitic steel and austenitic stainless steel have been joined by various researchers employing nickel-based filler. The nickel-based filler is preferred over other materials because of its intermediate coefficient of thermal expansion (CTE), high temperature creep strength and high corrosion resistance property. The carbon has low diffusion activity in nickel. Thus, the nickel-based filler restricts the carbon migration from ferritic steel to austenitic stainless steel. In addition, a nickel-based filler is less prone to solidification cracking. The nickel-based filler also provides a longer service life for the components than the austenitic filler. It has been reported that nickel-based filler increases the service life of the DWJs to 5 times compared to the austenitic filler [9]. Cao et al. [10] performed the GTAW of T92/Super304H dissimilar steel using ERNiCr-3 and ERNiCrMo-3 filler wires, and they reported that weld made using ERNiCrMo-3 welding wire has better mechanical and microstructural properties than ERNiCr-3 filler. The authors reported that the low toughness of the weld metal was due to the coarse dendritic austenitic microstructure. Nickel-based fillers such as ERNiCr-3, ERNiCrMo-3, ERNiCrMoCo-1, and ERNiFeCr-2 are commonly used due to their superior performance at elevated temperatures. Also, nickel-based filler provides good corrosion resistance to weld [11]. In the present work, ERNiCrMo-3 filler was used to join P92 steel and 304L ASS. The intermediate coefficient of thermal expansion value of the ERNiCrMo-3 filler, its high-temperature creep rupture strength, and high corrosion resistance make it suitable for joining dissimilar materials [12].

Fusion welding is one of the most popular joining processes used to fabricate parts in the automobile industry, power plants, nuclear and aerospace sector, petrochemical industry, and shipbuilding. The gas tungsten arc welding (GTAW) process is a universally used fusion welding process due to its high quality, productivity, and consistency.

The narrow groove geometry for the TIG welding method is one of the most economical methods to join dissimilar metals due to fewer passes required to fill the gap and less filler metal deposition required than the conventional V-groove joint [13]. The narrow groove design requires low heat input, and also use of this design results in less distortion and thermal stresses in weld joints than the conventional groove design [14]. However, the reduced gap between the plates to be joined in a narrow groove design makes it difficult for the welder to get proper access to the weld fusion zone. Thus, an expert welder is required for the welding with the narrow groove design. The defects such as lack of fusion may frequently occur during narrow groove welding if proper attention is not given [15]. The implementation of narrow groove design results in a significant reduction in costly nickel-based filler material consumption. The choice of the appropriate filler metal is important to get the defect-free weld joint. Jula et al. [16] performed TIG welding between P91 martensitic steel and AISI 316 SS using ERNiCrMo-3 filler. The authors reported the formation of secondary phases in the weld fusion zone due to the segregation of the alloying elements. The formation of filler-deficient regions such as beach, peninsula, and island was also found due to the difference in melting point of base metal and weld metal [17]. Shuo et al. [18] also performed the TIG welding of T92 and SS 304H using ERNiCrMo-3 filler. They reported that the formation of delta ferrite near the T92 fusion line has a detrimental effect, and PWHT improves the mechanical property. Li et al. [19] reported that the solid-state phase transformation (SSPT) influences the residual welding stresses. Hosseini et al. [20] found the microstructure and mechanical properties of TIG-welded Inconel 617 and AISI 310 SS using Inconel 617, Inconel 82, and 310 austenitic stainless steel filler materials. The authors concluded that the Inconel filler is superior to the austenitic filler as it provides better compatibility with the base metal and restricts carbon diffusion across the fusion boundary [21].

Apart from the mechanical property and microstructural characteristics evaluation, investigation of the residual stresses is required to ensure the safe working of the dissimilar material joint. The high tensile residual stress in HAZ of the P92 steel result in Type IV cracking and premature creep rupture of the P92 welded joint put into the service [19]. It should be noted that residual stresses do not always have a detrimental effect. It was reported that compressive residual stresses decrease the crack growth rate, while tensile residual stresses increase the stress concentration and intergranular stress corrosion cracking (IGSCC) during service life [22]. Among the various techniques available to reduce welding-induced residual stresses, the application of the narrow groove design is becoming popular nowadays. Taraphdar et al. [23] reported that a narrow groove configuration

reduces the peak longitudinal residual stress by 14% compared to the different conventional groove configurations. The mechanical and microstructural properties of the P92 steel change during the welding because of the high temperature experienced during the weld thermal cycle. Thus, PWHT is performed after welding to obtain the desired mechanical and microstructural properties. The PWHT also minimizes welding-induced residual stresses. From the several literatures reviewed, it was found that the formation of the sigma phases, laves phases, coarsening of the precipitates, high stresses at the weld interface, carbon migration, and low oxidation resistance of ferritic steel at high temperatures are the key problems which may lead to the sudden failure of these DWJs [9]. Thus, the present work will also be helpful for the researcher and reader to understand the effect of nickel-based filler on the mechanical, microstructural, and residual stresses properties of P92/304L SS DWJs. The effect of narrow shape groove profile is discussed in detail concerning microstructural changes, mechanical properties, and residual stresses. The through-thickness residual measurement in the weld fusion zone and heat-affected zone for the P92/304L SS DWJs using the deep hole drilling technique is completely a novel approach. The narrow groove geometry can be beneficial over conventional V-groove geometry due to the low included angle, thus the narrow groove design requires less welding time and less weld metal deposition. Also, a narrow groove design minimizes the weld distortion and residual stresses due to less volume of weld metal and low heat input.

## 2 Material and experimental details

### 2.1 Material

The normalized (1040 °C for 40 min and air-cooled) and tempered (760 °C for 2 h and air-cooled) P92 steel plate of thickness 10 mm was used in the experiments. The solution annealed (1100 °C for 20 min and air-cooled) AISI 304L SS plate was used for DWJs. The DWJs was performed using an ERNiCrMo-3 filler rod of a diameter of 2.4 mm. The optical emission spectroscopy (OES) result of this material is given in Table 1. The optical microscope (OM) and scanning electron microscope (SEM) microstructure of the P92 steel is shown in Fig. 1a, b. The microstructure mainly consists of tempered martensite and precipitates along the prior austenite grain boundaries (PAGBs). The Image J software was used for the grain size measurement. The average grain size of the P92 BM is  $20 \pm 1 \mu\text{m}$ . The normalizing and then air cooling produces a 100% martensitic microstructure. This martensitic microstructure is then tempered and air-cooled to soften the brittle and hard martensite produced after normalizing process. Figure 1c shows the OM

**Table 1** Composition of ERNiCrMo-3 filler metal, and P92 and SS 304L BM (wt-%)

Element (%wt.)	P92 steel	AISI 304L SS	ERNiCrMo-3 filler	ERNiCrMo-3 weld
C	0.093	0.018	0.012	0.022
Mn	0.41	1.12	0.37	0.047
P	0.019	0.024	0.008	0.004
S	0.004	0.011	0.001	0.004
Si	0.21	0.42	0.091	0.038
Cr	8.60	18.05	20.67	21.80
W	1.98	–	–	0.084
Mo	0.45	–	9.23	8.80
V	0.18	–	–	0.032
Fe	Rem	Rem	0.36	5.82
Nb	0.052	–	3.96	3.22
N <sub>2</sub>	0.060	–	–	–
Ni	0.31	8.06	64.89	58.38
Ti	0.001	–	0.12	0.29
Al	0.001	–	0.08	0.07
B	0.002	–	–	–
Zr	0.002	–	–	–
Cu	–	–	0.01	0.016
Cr <sub>eq</sub>	<b>9.391</b>	<b>18.68</b>	<b>32.2565</b>	<b>32.847</b>
Ni <sub>eq</sub>	<b>3.305</b>	<b>9.16</b>	<b>65.435</b>	<b>59.0635</b>
Cr <sub>eq</sub> /Ni <sub>eq</sub>	<b>2.841</b>	<b>2.039</b>	<b>0.493</b>	<b>0.556</b>

Cr<sub>eq</sub> value represents the chromium equivalent value, Ni<sub>eq</sub> value represents the nickel equivalent value and Cr<sub>eq</sub>/Ni<sub>eq</sub> value represents the ratio of chromium equivalent for P92 steel, 340L SS steel and ERNiCrMo-3 filler, and weld metal. The less one value of Cr<sub>eq</sub>/Ni<sub>eq</sub> indicates the austenitic microstructure

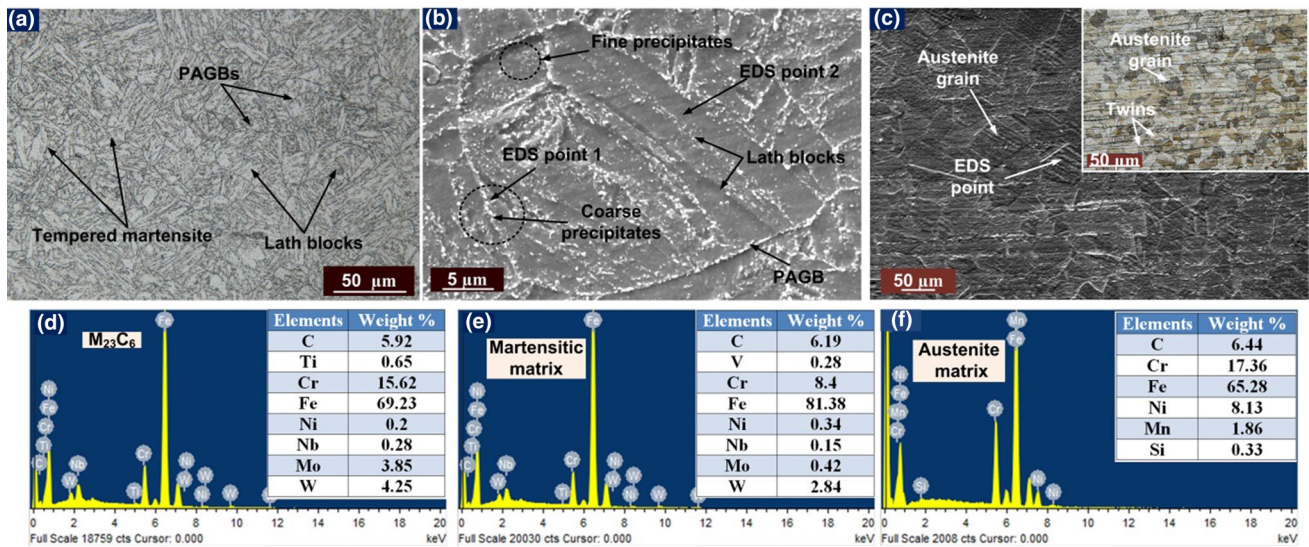


**Fig. 1** a OM image of P92 BM, b SEM image of P92 BM, c OM image of 304L SS BM, d EDS spectrum of coarse white precipitates (M<sub>23</sub>C<sub>6</sub>) at PAGBs e EDS spectrum of base metal matrix and f EDS spectrum of austenite grain

and SEM image of the as-received 304L SS. The 304L SS consists of austenite grains and annealing twins. The average grain size of the austenitic grain is 32 ± 1 μm. The P92 steel consists of coarse precipitates M<sub>23</sub>C<sub>6</sub> (M=Fe, Cr) carbides along PAGB and fine precipitates MX (M=Nb, V;

X=N, C) carbonitrides along intra-lath regions. Based on the TEM images of the M<sub>23</sub>C<sub>6</sub> and MX particles, the mean size of M<sub>23</sub>C<sub>6</sub> type precipitates was reported in the range of 80–100 nm, while the mean size of MX-type precipitates was reported in the range of 20–40 nm [24]. The energy

dispersive spectroscopy (EDS) peak of the Fe, Cr, V, and Nb elements is shown in Fig. 1d, e shows the  $M_{23}C_6$  and MX precipitates along PAGB and intra-lath regions. The precipitation of the vanadium nitrides during the tempering improves the creep strength of the P92 steel by restricting the movement of the dislocations [25]. The chromium equivalents ( $Cr_{eq}$ ) and nickel equivalents ( $Ni_{eq}$ ) are used to identify austenitic, martensite, or ferritic phase stability. The Schaeffler diagram is shown in Fig. 2. The ratio of  $Cr_{eq}$  and  $Ni_{eq}$  is used to identify the mode of the solidification (austenitic or ferritic or both). For  $Cr_{eq}/Ni_{eq} < 1.25$ , the fully austenitic mode of solidification takes place [26]. For ERNiCrMo-3 weld metal, the ratio of  $Cr_{eq}$  and  $Ni_{eq}$  was found to be 0.559. The Schaeffler formula presented the  $Cr_{eq}$  and  $Ni_{eq}$  equivalents as given in Eqs. (1) and (2) [27]. The modified Schaeffler formula [28] is given in Eqs. (3) and (4). According to the Schaeffler equation, the  $Cr_{eq}$  and  $Ni_{eq}$  calculated for P92 steel, 304L SS, ERNiCrMo-3 filler, and ERNiCrMo-3 weld are listed in Table 1. According to the Schaeffler formula, P92 steel come in the martensitic range as shown in Fig. 2. However, as P92 is ferritic–martensitic creep-strength steel, the modified Schaeffler formula was also used. According to the modified Schaeffler formula, P92 steel comes in the ferritic-martensitic range as shown in Fig. 2. For 304L SS and ERNiCrMo-3 filler metal, Schaeffler formula was only used. The formula used for various materials is marked in Fig. 2.

$$Cr_{eq} = Cr + Mo + 1.5(\%Si) + 0.5(\%Nb) \tag{1}$$

$$Ni_{eq} = Ni + 30(\%C) + 0.5(\%Mn) \tag{2}$$

$$Cr_{eq} = Cr + 1.5(\%Mo) + 2(\%Si) + 5(\%V) + 5.5(\%Al) + 1.75(\%Cb) + 1.5(\%Ti) + 0.75(\%W) \tag{3}$$

$$Ni_{eq} = Ni + Co + 30(\%C) + 0.5(\%Mn) + 0.3(Cu) + 25(\%N) \tag{4}$$

### 2.2 Experimental procedure

The rectangular plates with dimensions 150 mm × 55 mm × 10 mm were machined from each base metal for the welding experiments. The test plate thickness, length, and width were decided by considering the dimensions of various test specimens like Charpy, tensile and residual stress measurement required (Fig. 3). Also, the dimensions were decided so that there is less material wastage. A Lincoln (Model: Precision TIG 225) gas tungsten arc welding equipment was used to produce a narrow groove multipass TIG welded joint. The tungsten electrode (EWTh-2, 2% Thoriated) of diameter 3.2 mm was used for the welding. The pure argon (purity: 99.995%) gas was used as a shielding gas. The shielding gas was

Fig. 2 Schaeffler diagram [29]

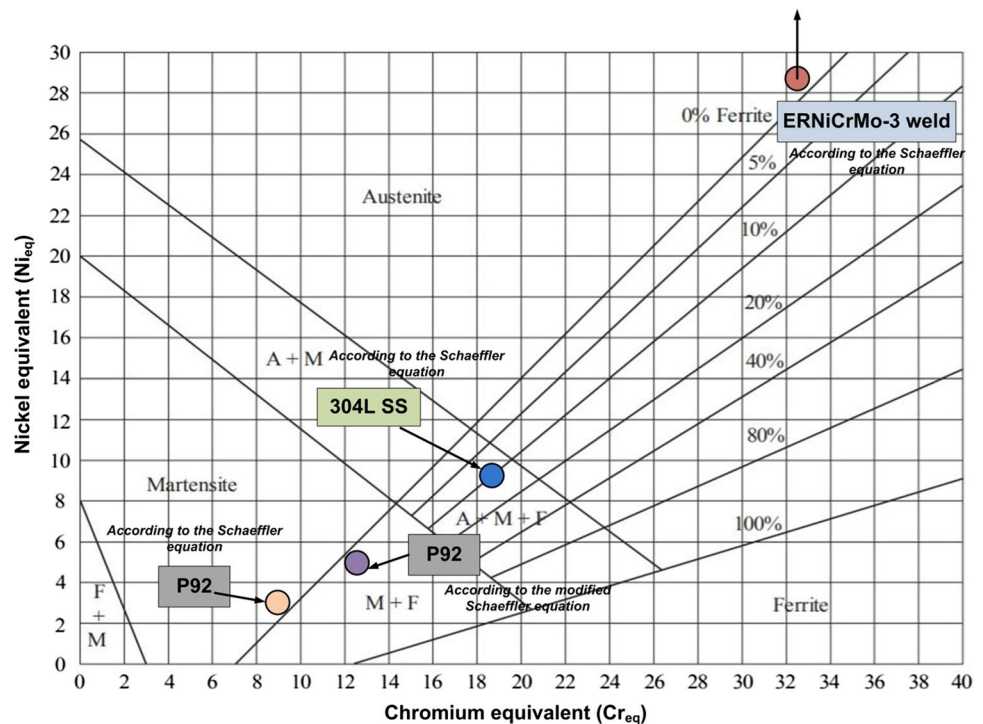
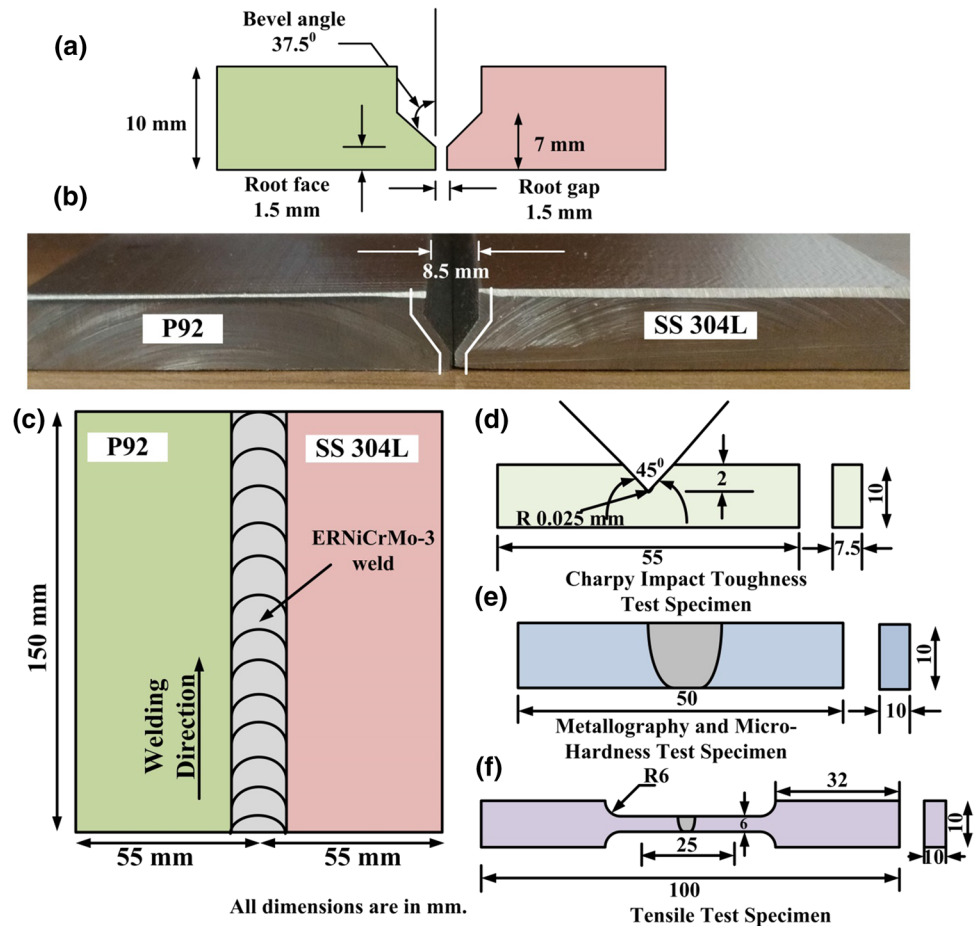


**Fig. 3** **a** Schematic drawing of the narrow groove configuration, **b** Narrow groove joint preparation on P92 and 304L SS plate, **c** Schematic diagram of the welded plate, **d** Specimen dimension for Charpy test, **e** Specimen dimension for metallography examination, **f** Specimen dimension for tensile test



supplied at a flow rate of 15 L/min. The schematic diagram of the narrow groove geometry formed on the P92 and 304L SS plate is shown in Fig. 3a, b. Before the joining, the plates were cleaned using acetone to remove the dust, oil, moistures, and other impurities present on the surface of the base metal to ensure a defect-free weld. The schematic drawing of the welded plate is shown in Fig. 3c. After welding, specimens for the Charpy test, metallography examination, and tensile test were taken from the transverse direction of the weld by following the standard sample preparation procedure as shown in Fig. 3d–f. The welding parameters and heat input for each welding pass

is given in Table 2. Prior to the actual welding, both the base plates were tack welded at three different locations using the current of 120 A, as shown in Fig. 4a. The tack weld prevents the misalignment and ensures the appropriate gap between the two plates to be welded. After tacking, the P92 plate was preheated up to the temperature of 200 °C with the help of flame heating to avoid cold cracking and to control the hydrogen diffusion into the molten pool, as shown in Fig. 4b. The preheating temperature of 200 °C and inter-pass temperature of 250 °C are recommended for P92 steel [30]. The temperature was monitored with the help of an infrared (IR) temperature

**Table 2** Welding process parameters

Pass number	Welding Parameters			Average heat input per unit length per pass (kJ/mm)	Total heat input per unit length of the weld (kJ/mm)
	Current (A)	Voltage (V)	Average welding Speed (mm/min)		
Root pass	155	~16.7	~98	0.95	3.62
Filler pass	145	~16.2	~95	0.89	
Capping pass	145	~16.2	~95	0.89	
Backing pass	145	~16.2	~95	0.89	

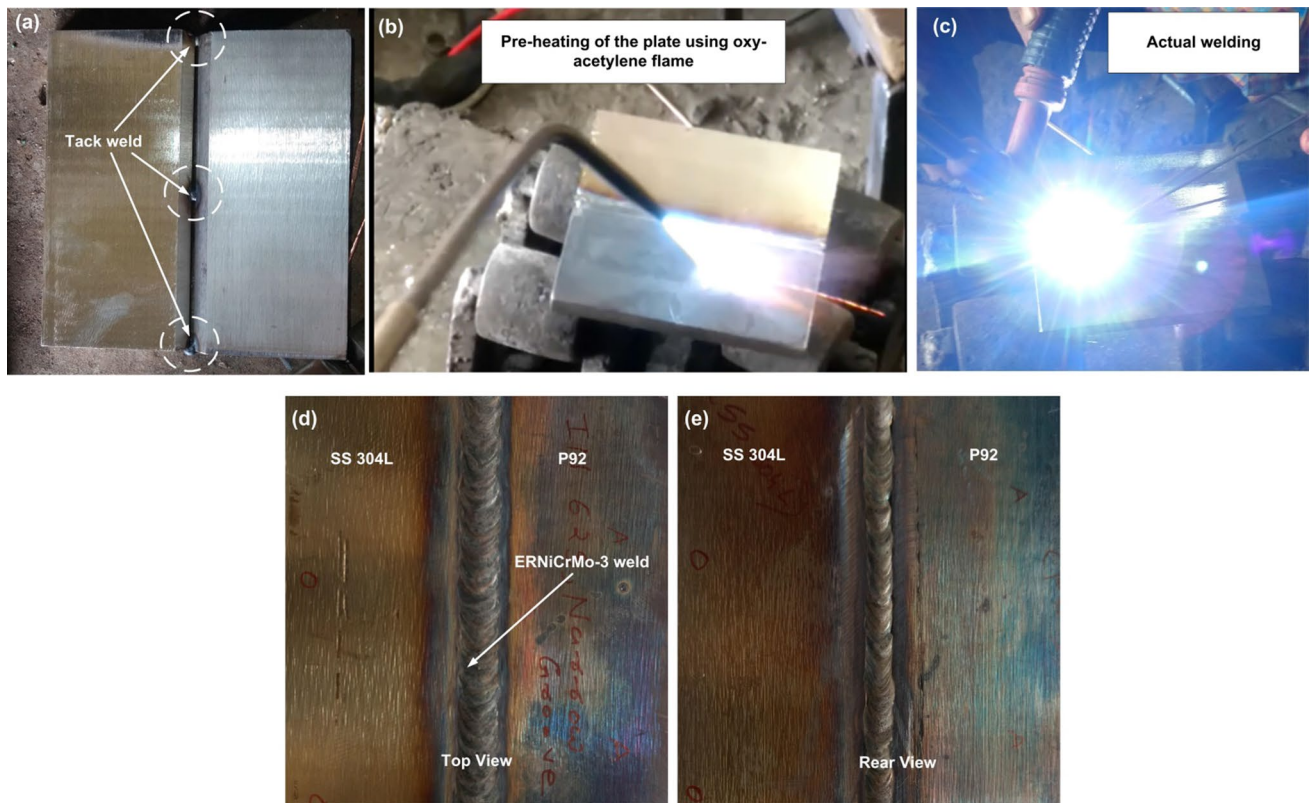


**Fig. 4** a Tack weld at three different locations, b preheating of the P92 plate, c Actual TIG welding using ERNiCrMo-3 filler, d Top view of the DWJ, e Rear view of the DWJ

gun. After preheating, a welding pass is performed by a qualified welder, as shown in Fig. 4c. The top and rear view of the welded plate is shown in Fig. 4d. The welding was performed without clamping the plates to minimize the residual stress build-up. However, it resulted in a minor distortion of the welded plate. The welding was performed without ceramic backing. However, the copper strip was placed on the backside of the joint. Also, back chipping was performed after welding to achieve the required penetration.

For metallographic studies, coupons were prepared by grinding using 80, 120, 180, 220, 320, 400, 600, 800, 1000, 1200, and 1500 grits of SiC paper, followed by the final polishing with 1  $\mu\text{m}$  alumina powder slurry. The ERNiCrMo-3 weld fusion zone was electrolytically etched with 10% oxalic acid solution (10gm oxalic acid + 100 ml water, time-30 s) at current density and voltage of 1  $\text{A}/\text{cm}^2$  and 4 V, respectively. Then, villeda's solution (1 g picric acid + 5 ml hydrochloric acid + 100 ml of ethanol) was used for the P92 side, and glyceresia (10 ml  $\text{HNO}_3$  + 20 ml glycerol + 30 ml HCL) for the SS 304L side. The Leica DMC4500 OM and EVO 18 Carl Zeiss SEM were used for microstructure studies.

The micro-hardness value was recorded at an interval of 1 mm (the interval was reduced to 0.25 mm for the P92 HAZ region to get the precise micro-hardness value of the CGHAZ, FGHAZ, and ICHAZ region) by applying a load of 500 g and dwell time of 10 s using semi-automatic microhardness tester. The tensile test coupons were prepared according to the ASTM-E8 standard. The tensile test was performed on the 100KN capacity INSTRON 5980 universal testing machine at room temperature with a 1 mm/min strain rate. The Charpy V-notch impact toughness test was carried out at room temperature using an impact tester with the 55 mm  $\times$  10 mm  $\times$  7.5 mm standard specimens for welded specimens. The heat input for each welding pass was calculated by using Eq. (5), considering arc efficiency as 60% for the GTAW welding.

$$Q = \frac{\eta VI}{s}, \quad (5)$$

where " $\eta$ " is the heat transfer efficiency, " $V$ " is arc voltage in volts (V), " $I$ " is welding current in amperes (A), " $s$ " is welding speed in mm/s.

### 2.3 Residual stress measurements procedure

The deep hole drilling (DHD) method is the most commonly used experimental technique for measuring welding-induced residual stresses. The DHD method is classified as a destructive method for the measurement of welding-induced residual stresses. In this method, a small reference hole of diameter 3 mm is created with the help of the EDM tool. The DHD method involves the measurement of reference hole diameter before and after trepanning. Then in the next step, the diameter of this reference hole is measured with the help of an air probe system at various locations. In the third step, another hole with an internal diameter of 8 mm and outer diameter of 12 mm is coaxially trepanned using an EDM drilling machine. In the fourth step, the diameter of the reference hole is re-measured after trepanning. The change in reference hole diameter gives the value of the strain. The change in reference hole diameter is due to the stress relaxation that occurred due to the removal of material. This strain is then converted into stress by using various analytical equations [23]. The strain gauge was used to determine the strain value at a different point. The data logger was used to record the strain value at different locations. The DHD method was employed to determine the residual stress distribution across the weld zone and the HAZ as shown in Fig. 5a. The four essential steps of the DHD technique are shown in Fig. 5b. The detailed analytical equations and theory of the DHD technique used for the residual stress analysis are available in the following reference [31]. Equations 6 and 7 were used to calculate the longitudinal and transverse residual stress

magnitudes, respectively [32]. The  $\epsilon_x$  and  $\epsilon_y$  represents the strain in the longitudinal and transverse directions. The  $\Delta d_x$  represents the change in the diameter of the reference hole before and after trepanning. The modulus of elasticity ( $E$ ) was taken as 250 GPa for the P92 steel [33]. The calculated strain value in longitudinal and transverse directions for the ERNiCrMo-3 weld, P92 HAZ, and 304L SS HAZ is given in Table 3. The corresponding longitudinal and transverse stress value are listed in Tables 4, 5).

$$\epsilon_x = \frac{\Delta d_x}{d_x} = -\frac{1}{E} [3\sigma_x - \sigma_y] \tag{6}$$

$$\epsilon_y = \frac{\Delta d_y}{d_y} = -\frac{1}{E} [3\sigma_y - \sigma_x] \tag{7}$$

## 3 Results and discussion

### 3.1 Radiographic examination

The non-destructive technique, known as X-ray radiographic inspection, was conducted to identify the defects such as porosity, crack, and surface defects that may be present inside the weld fusion zone and which are not visible through necked eyes. The radiographic examination was conducted according to the standard procedure mentioned in ASME Sec-V Article 2 & 22, 2017. The acceptance

**Fig. 5** a P92/304L SS DWJs prepared for residual stress analysis using DHD technique. b Schematic diagram of the DHD method

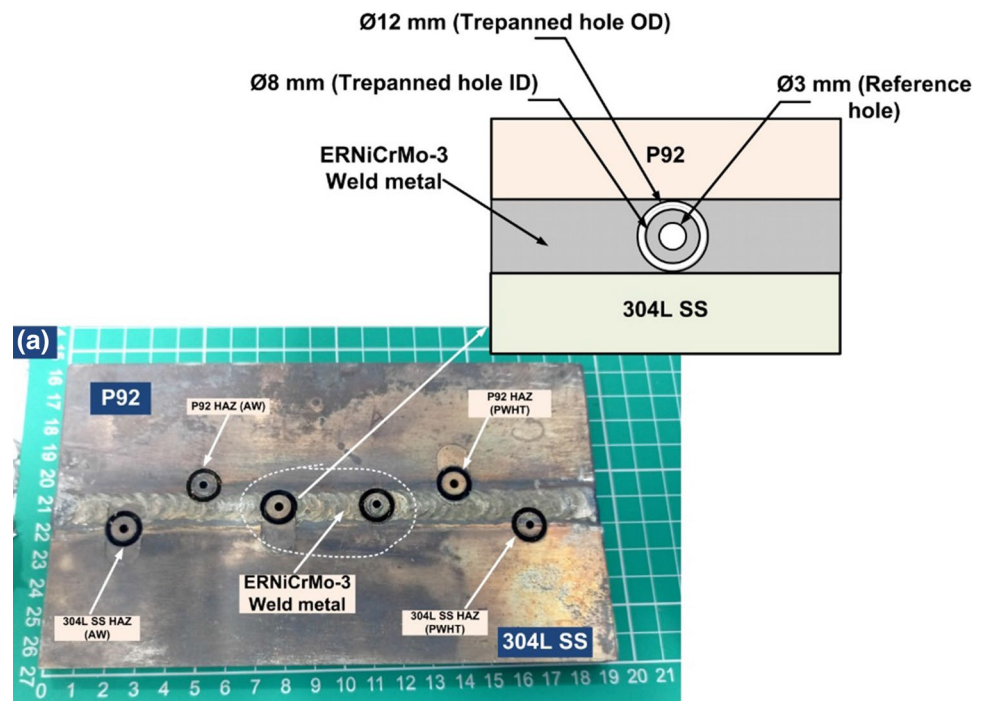
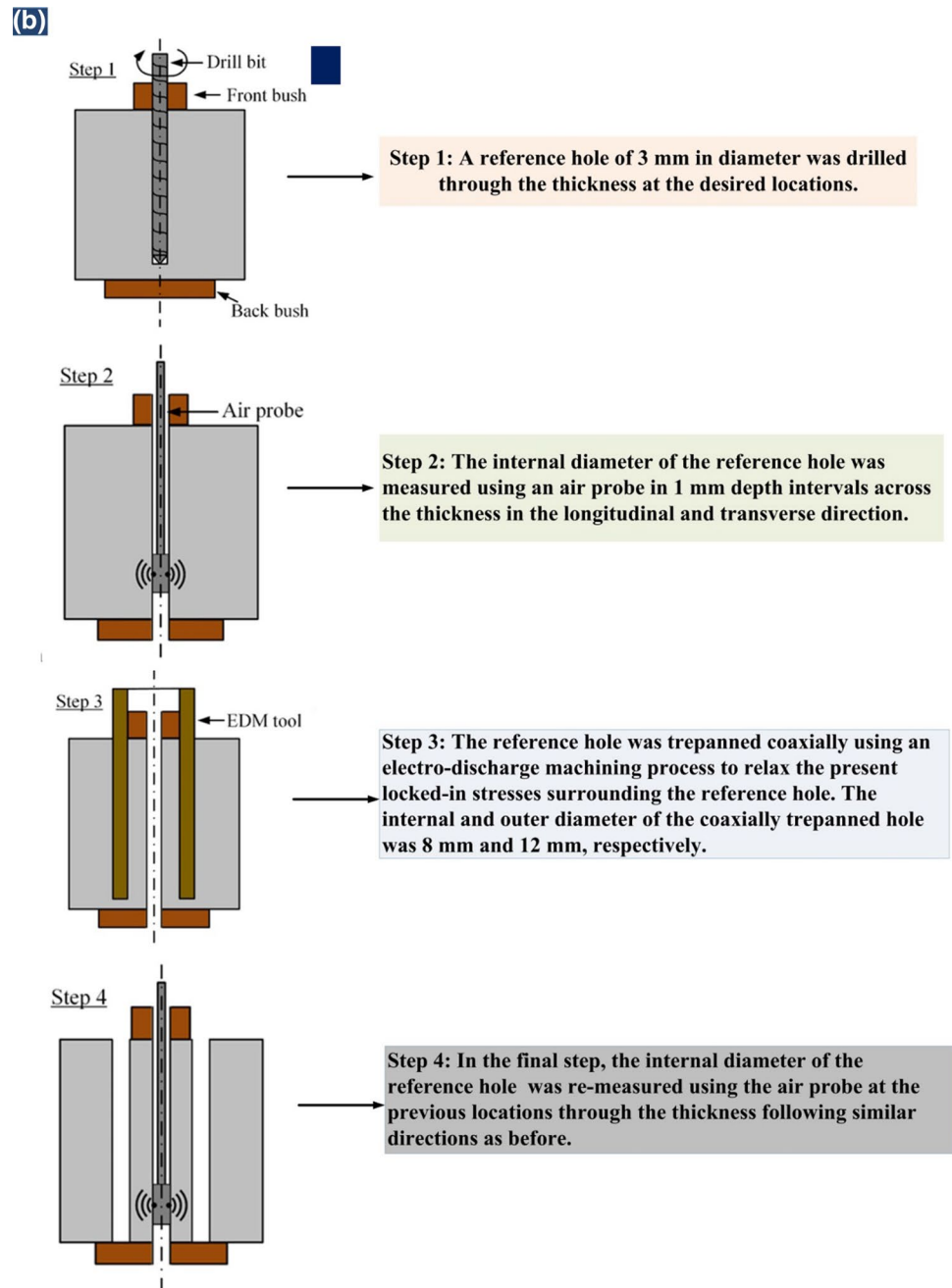




Fig. 5 (continued)



condition was as per the ASME Sec-IX (QW-191.1.2). The radiographic examination was conducted using an Ir-192 (Iridium) source. The total exposure time for this test was 2 min, and the processing time of the radiographic film was 3–5 min. The radiograph of the weld bead obtained using the X-ray radiography technique is shown in Fig. 6. The radiograph revealed no significant defects in the weld bead, so the welding procedure and parameters were qualified and the sample was accepted for further investigation of the mechanical and microstructure properties.

### 3.2 Macrostructure study

The macrostructure of the P92 and 304L steel plate welded using ERNiCrMo-3 filler metal is shown in Fig. 7. The macrostructure indicates the good fusion of the base and filler metal. The macrostructure image confirms no significant defect in the dissimilar joint and thus confirms the x-ray radiographic result. The weld fusion zone, HAZ, and base metal are clearly indicated in the macrograph. The various measurements performed towards the HAZ and

**Table 3** Strain value for the ERNiCrMo-3 weld, P92 HAZ, and 304L SS HAZ in the AW state

ERNiCrMo-3 weld		P92 HAZ		304L SS HAZ	
Strain In X-X (Longi.)	Strain In Y-Y (Trans.)	Strain In X-X (Longi.)	Strain In Y-Y (Trans.)	Strain In X-X (Longi.)	Strain In Y-Y (Trans.)
-0.00139	0.00023	0.00212	0.00084	-0.00153	0.00033
-0.00136	-0.00036	0.00228	0.00254	-0.00206	-0.00069
-0.00082	-0.00083	0.00293	-0.00118	-0.00209	-0.00119
-0.00036	-0.00152	0.00355	0.00102	-0.00109	-0.00126
0.00032	-0.00132	0.00356	0.00138	0.00158	-0.00116
0.00105	-0.00016	0.00281	0.00196	0.00221	-0.00039
0.00139	0.00026	0.00122	0.00225	0.00348	0.00039
0.00166	0.00049	0.00133	0.00248	0.00481	0.00033
0.00156	0.00069	0.00036	0.00154	0.00296	-0.00149
0.00133	0.00073	0.00172	0.00095	0.00302	-0.00076

**Table 4** Residual stress data for ERNiCrMo-3 weld fusion zone

Thickness (mm)	As-welded		After PWHT	
	Longitudinal (MPa)	Transverse (MPa)	Longitudinal (MPa)	Transverse (MPa)
1	241	90	41	-77
2	266	101	49	-83
3	269	83	29	-72
4	249	72	15	-92
5	225	77	9	-89
6	197	-14	-21	-77
7	174	-55	-75	-68
8	154	-79	-68	-51
9	39	-92	-69	-41
10	-31	-88	-97	-39

**Table 5** Residual stress data for P92 HAZ

Thickness (mm)	As-welded		After PWHT	
	Longitudinal (MPa)	Transverse (MPa)	Longitudinal (MPa)	Transverse (MPa)
1	-165	-98	-181	42
2	-137	-111	-211	52
3	-92	-81	-191	61
4	-71	-69	-225	49
5	-59	-71	-218	36
6	-49	-82	-198	38
7	-31	-69	-149	56
8	-42	-58	-131	36
9	-58	-61	-66	40
10	-24	-41	-61	31

along the weld fusion zone are shown in Fig. 7. The Image J software was used to measure the macrostructure cross-sectional area, HAZ area, and HAZ width. The measured area of the weld fusion zone with reinforcement was  $67 \pm 1 \text{ mm}^2$ . The measured area of the HAZ toward the P92 side was  $35 \pm 1 \text{ mm}^2$ . Due to the higher thermal conductivity of the P92 steel compared to the 304L SS; HAZ of width 4.52 mm was recorded at the P92 side. Because of the low thermal conductivity of the 304L SS, negligible HAZ was formed towards the 304L side.

### 3.3 Microstructural characterization

#### 3.3.1 Characterization of heat-affected zone in as-weld state and after PWHT

In P92-304L SS DWJs, HAZ is the region that needs special attention due to its changing metallurgical and mechanical properties compared to the base metal and weld fusion zone. HAZ is a region that is not melted during the welding process but experiences such a high temperature during the welding that mechanical and metallurgical properties changes take place in this region. Also, sometimes high residual stresses are generated in this region, which weakens this region compared to the BM and weld fusion zone. As shown in Fig. 8, according to grain morphology, P92 HAZ can be separated into three different regions, that is, CGHAZ, FGHAZ, and ICHAZ. The CGHAZ undergoes the approximate maximum temperature of  $1300 \text{ }^\circ\text{C}$  (much above the upper critical temperature  $Ac_3 \sim 1040\text{--}1080 \text{ }^\circ\text{C}$ ) during the welding. Due to such a high temperature, precipitates dissolve in the austenitic matrix, and thus pinning effect of these precipitates does not occur. Thus, precipitates are unable to restrict the movement of grain boundaries. During the welding, the tempered martensite transform into the

**Fig. 6** Radiograph of the weld bead

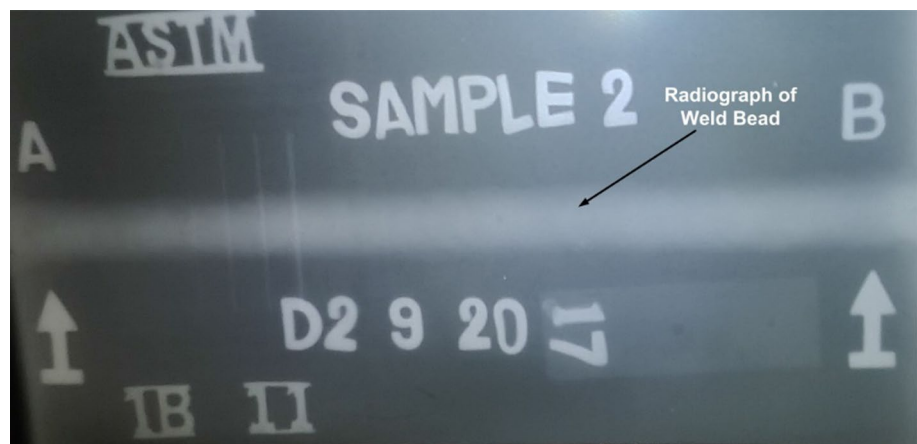
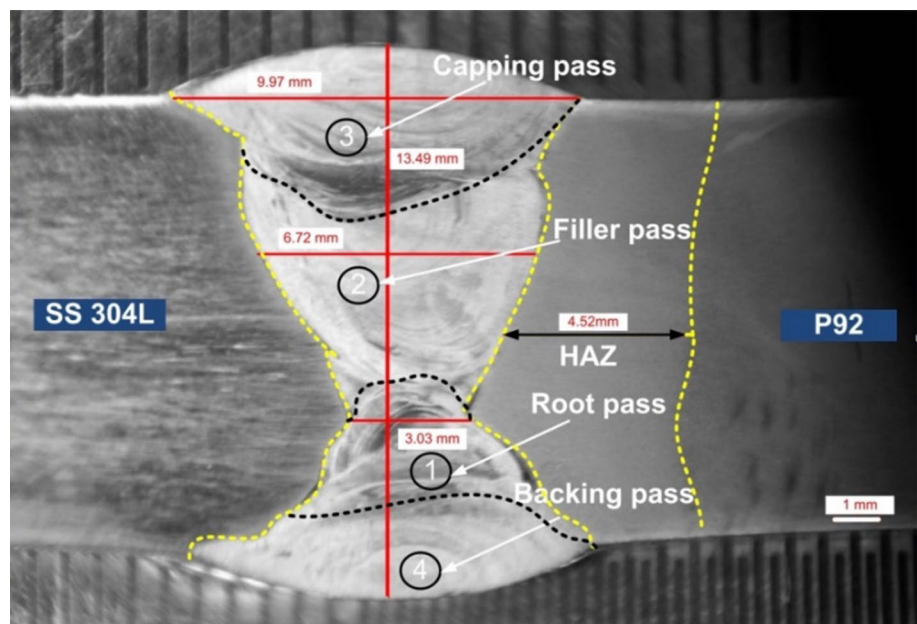


**Fig. 7** Macrostructure of the P92 and 304L SS welded joint



austenite phase as it experiences a temperature higher than the  $A_{c3}$ . At this temperature,  $M_{23}C_6$  and MX precipitates dissolve to promote grain growth. Thus, coarse austenite grain growth takes place, and soon after the welding (during cooling) this coarse austenite phase is converted into martensite, thus CGHAZ is formed. The CGHAZ mainly consists of coarse prior austenite grains and untempered lath martensite. The optical and SEM image confirms the absence of precipitates along the PAGBs, packet boundaries (PBs), and block boundaries (BBs). On cooling after welding, some austenite grain was transformed into the delta ferrite since its cooling rate is very high. The  $\delta$ -ferrite phase was formed near the P92 and WM interface. Some previous works [34] also observed the detrimental  $\delta$ -ferrite phase near the weld fusion zone. Figure 8 shows the micrograph of the P92 and WM interface and P92 HAZ in the as-welded situation. The region adjacent to the CGHAZ is FGHAZ. The FGHAZ

experiences a temperature slightly above the  $A_{c3}$ . Thus, unlike the CGHAZ, not all the precipitates completely dissolve inside the matrix, but some fine precipitates dissolve, and few coarse precipitates survive. These undissolved precipitates restrict the movements of the grain boundary and thus prevent the coarse austenite grain growth. This results in the formation of the fine prior austenite grains. Some undissolved precipitates are visible in the SEM image shown in Fig. 9. The region close to the FGHAZ is ICHAZ. The ICHAZ experiences the temperature between the lower critical temperature ( $A_{c1}$ ) and  $A_{c3}$ . Thus, only partial transformation of the austenite phase occurs. During cooling, this austenite phase formed transforms into martensite [35]. The average prior austenite grain size for CGHAZ in as-welded conditions was  $11 \pm 1 \mu\text{m}$ . The SEM image of the P92 HAZ and weld interface is shown in Fig. 9. The SEM image shows the soft ferrite zone near the fusion line. The microstructure

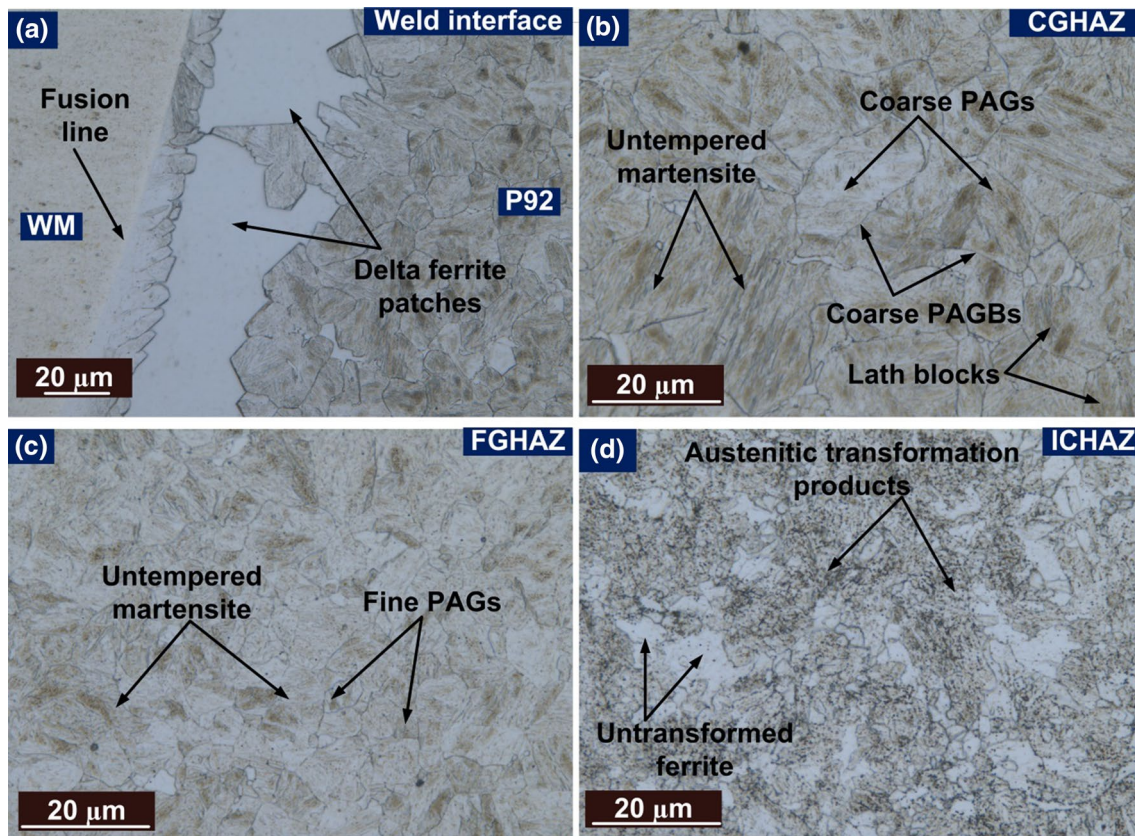


**Fig. 8** In as-weld condition **a** OM image of the P92 HAZ and weld interface, **b** CGHAZ, **c** FGHAZ, **d** ICHAZ

observed using SEM across the CGHAZ, FGHAZ, and ICHAZ is shown in Fig. 9b–d. The SEM micrograph of the CGHAZ shows the coarse prior austenite grains, untempered martensite lath structure, and dissolution of carbide ( $M_{23}C_6$ ) and carbonitride (MX) precipitates. It is reported that above 900 °C most of the  $M_{23}C_6$  precipitates completely dissolve [36]. The FGHAZ shows the fine prior austenite grains and few undissolved precipitates.

The varying microstructure formed towards the P92 side during the welding can be homogenized by using the PWHT process. The PWHT homogenizes the mechanical property and microstructure of this critical region. The  $M_{23}C_6$  and MX particles generally precipitate in P92 steel after post-weld heat treatment known as tempering. These are the shining tiny white particles. However, during the weld thermal cycle due to the high temperature these particles are dissolved into the matrix. The PWHT is necessary for the evolution of the precipitates dissolved during the welding. These precipitates improve the creep strength by stopping the movement of the dislocations during creep. The PWHT is generally carried out below  $Ac_1$  to avoid the formation of fresh martensite. Obiko et al. [37] reported the

$Ac_1$  and  $Ac_3$  of the P92 steel in the range of 800–830 °C and 900–945 °C, respectively, using ThermoCalc analysis. They also reported that  $M_{23}C_6$  precipitates dissolve at a temperature of 870–888 °C, while MX precipitates dissolve at 1201–1250 °C. Maddie et al. [38] found that PWHT (tempering) at 760 °C gives good microstructure stability and high creep rupture time for the P92 steel operating at a temperature of 600 °C. According to the ASME code, PWHT temperature should not be less than 730 °C. In this study, PWHT, known as tempering, was performed at 760 °C, 2 h followed by air cooling. From Fig. 10a, it is clear that PWHT has no effect on the delta ferrite present at the interface. After PWHT, the coarse precipitates (black color in OM image and white color in SEM image) decorate along the prior austenite grain boundary and fine precipitates inside the PBs and BBs. Figure 10b–d shows the CGHAZ, FGHAZ and ICHAZ after PWHT. The SEM image of the P92 HAZ after PWHT is shown in Fig. 11. The decoration of the coarse carbide precipitates on PAGBs and subgrain boundaries confirms the reprecipitation of the precipitates after PWHT. The coarse  $M_{23}C_6$  precipitates were decorated

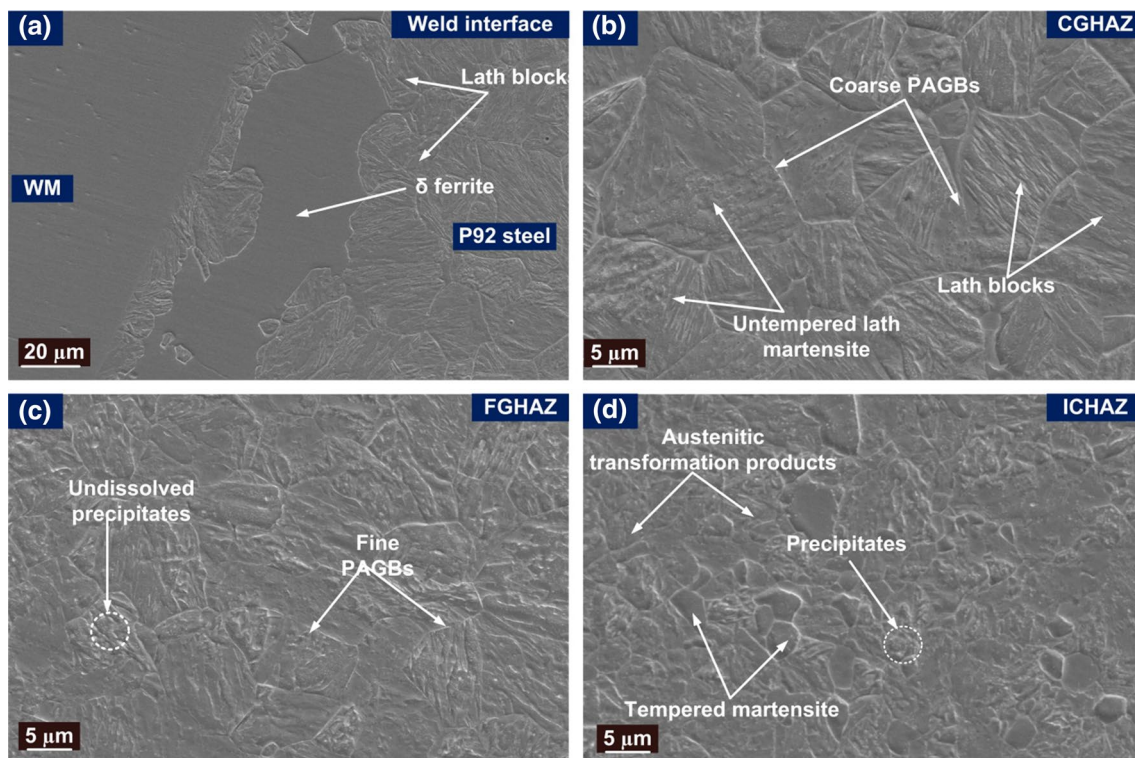


**Fig. 9** In as-weld condition **a** SEM image of P92 HAZ and weld interface, **b** CGHAZ, **c** FGHAZ, **d** ICHAZ

along the PAGBs, and sub-grain boundaries, as shown in Fig. 11b. The fine MX precipitates were observed in intralath regions after PWHT. This formation of the precipitates after PWHT provides the precipitation strengthening to the P92 steel. The welding results in the complete dissolution of these precipitates, and thus, PWHT becomes necessary after welding. The temperature is the critical PWHT parameter. The PWHT at a very low temperature will result in low toughness due to insufficient tempering, while the PWHT at a very high temperature will result in a reduction in the creep strength due to over-tempering [39]. Thus, the optimized PWHT parameter of 760 °C, 2 h is most commonly used. However, the problem associated with this PWHT parameter is the formation of the soft zone having a low micro-hardness value known as ICHAZ. ICHAZ is most prone to type IV cracking due to its complex microstructure. The average prior austenite grain size for CGHAZ in PWHT condition was  $9 \pm 1 \mu\text{m}$ .

The HAZ microstructure of the 304L SS in the as-welded condition is shown in Fig. 12. The 304L SS material has excellent corrosion resistance due to the high level of chromium. The chromium forms a protective oxide film on the surface and hence resists corrosion. This oxide film

regenerates when it is damaged, thus makes the 304L steel stainless. But during the welding or heat treatment, chromium precipitates as  $M_{23}C_6$  or  $M_7C_3$  carbides (M is metal and mainly chromium); thus, chromium depleted zone is formed at grain boundaries due to the carbide precipitation; this may result in the sensitization of the steel. The HAZ for the 304L SS did not show any distinguish microstructural features like P92. The microstructure study revealed the ferrite stringer near the fusion line. The ferrite stringer is formed due to the segregation of chromium. The EDS analysis of the ferrite stringers showed the enrichment of the Cr and Ni elements. The ferrite stringer is formed due to the rejection of the Cr from the austenitic matrix. Thus, the corrosion resistance of the 304L SS is affected due to the formation of the ferrite stringer. The ferrite stringer does not have any detrimental effect on mechanical properties in most of the applications. The heat treatment condition for the as-received austenitic 304L SS is annealing, followed by the water quenching after the hot rolling process; thus, no secondary precipitates are present in the microstructure of the base metal. Thus, welding and PWHT do not alter the microstructure of the 304L SS.

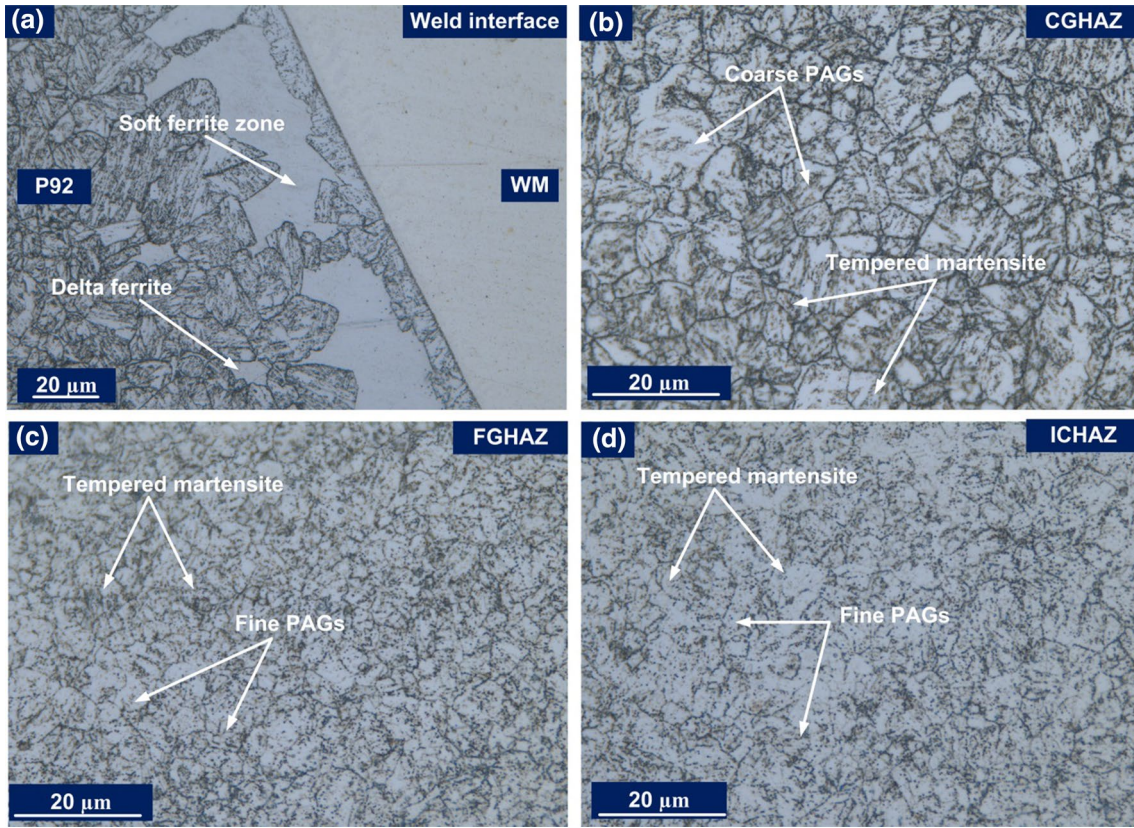


Fig. 10 After PWHT a OM image of the P92 HAZ and weld interface, b CGHAZ, c FGHAZ, d ICHAZ

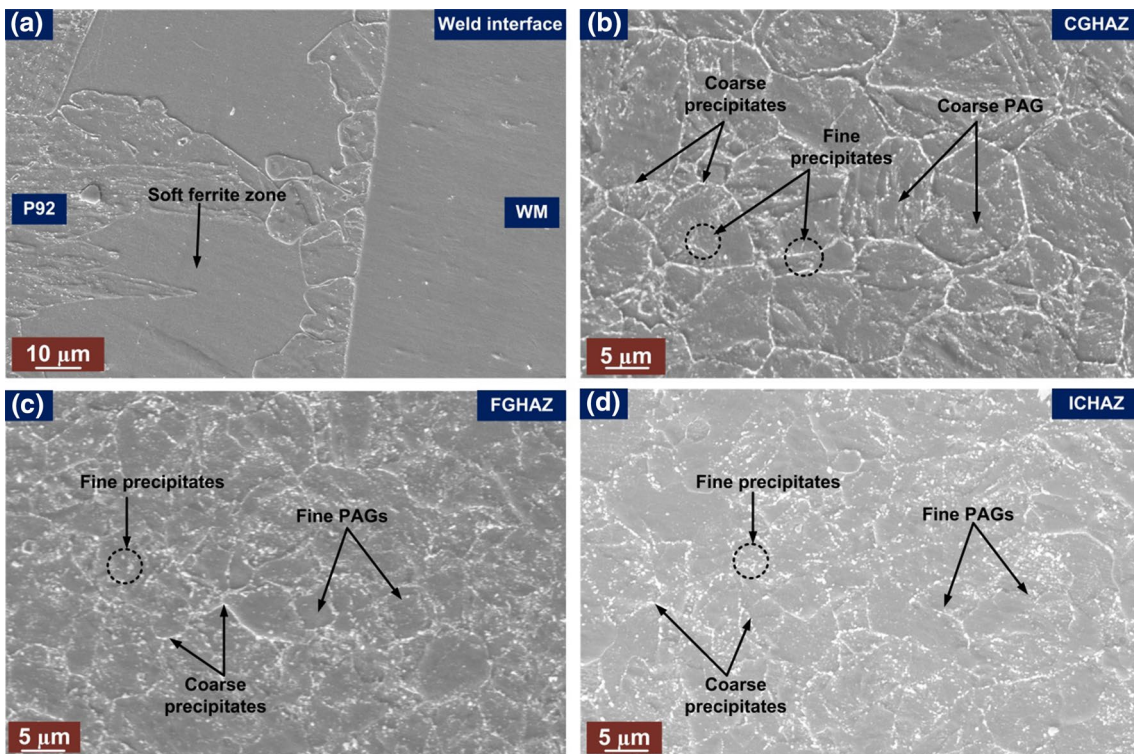
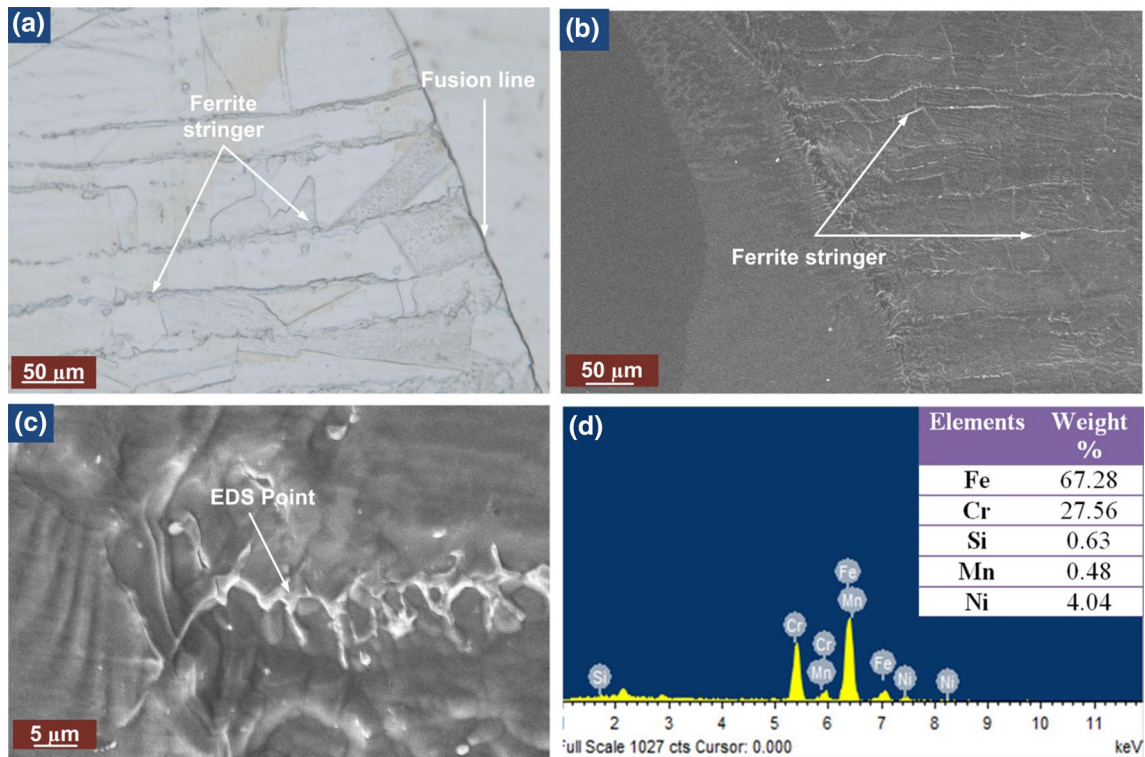


Fig. 11 After PWHT a SEM image of P92 HAZ and weld interface, b CGHAZ, c FGHAZ, d ICHAZ



**Fig. 12** In as-weld condition **a** OM image of 304L SS HAZ and weld interface, **b** SEM image of a micrograph of 304L SS HAZ and weld interface, **c** SEM image of 304L SS HAZ, **d** EDS spectrum of ferrite stringer

### 3.3.2 Microstructure characterization of weld interface and weld center

The ERNiCrMo-3 weld fusion zone microstructure is presented in Fig. 13. The austenitic microstructure mainly consists of columnar, cellular, and equiaxed dendrites. The existence of the unmixed zone at the interface of the weld fusion boundary and base metal is clearly visible in Fig. 13a, b. The unmixed zone is formed due to the variation in the chemical composition and melting point of the filler metal and base metal to be joined. The formation of beach, peninsula and island as shown in Fig. 13c depends on two important parameters: liquidus temperature of the base metal ( $T_{LB}$ ) and weld metal ( $T_{LW}$ ). If the  $T_{LW} < T_{LB}$ , complete mixing may occur but if the filler metal makes  $T_{LW} > T_{LB}$ , complete mixing is impossible [40]. The variation in the elements like nickel (Ni), chromium (Cr), and iron (Fe) between the two materials to be joined play a major role in the formation of the unmixed zone. The unmixed zone in the form of peninsula, and island are formed due to the faster cooling rate (low heat input during welding at that particular region), weld pool stimulation due to multipass welding, and a superior melting range of the filler metal compared to the base metal. The weld fusion microstructure shows columnar dendritic structure near the fusion

boundary, whereas the weld center shows an equiaxed dendritic structure. Figure 13a–h show the optical microstructure of the various zones of the weld fusion zone, like weld center, weld interfacial region, and near the fusion boundary. The different cooling rates at the weld center and at the weld interface result in the formation of columnar and cellular dendrites. The formation of fine equiaxed grains in weld fusion has many advantages, such as less susceptibility to solidification cracking, superior mechanical properties, high ductility, and fracture toughness.

The microstructure of the weld fusion zone was also analyzed using SEM, as shown in Fig. 14. In the dissimilar welding between two different metals, there exists a region between the fusion boundary and the base metal, which has a different composition and sometimes also different properties and microstructure than that of the bulk weld metal known as the unmixed zone, partially melted zone, and filler deficient region. The unmixed zone is that portion of the base metal that is melted during the welding process but solidifies without experiencing appropriate dilution with the filler metal. The unmixed zone was formed on both sides of the base metal, as shown in Fig. 14a, b. The composition of this unmixed zone differs from that of the base metal and bulk weld metal. The EDS results of the unmixed zone, as shown in Fig. 15 indicated that the unmixed zone has a

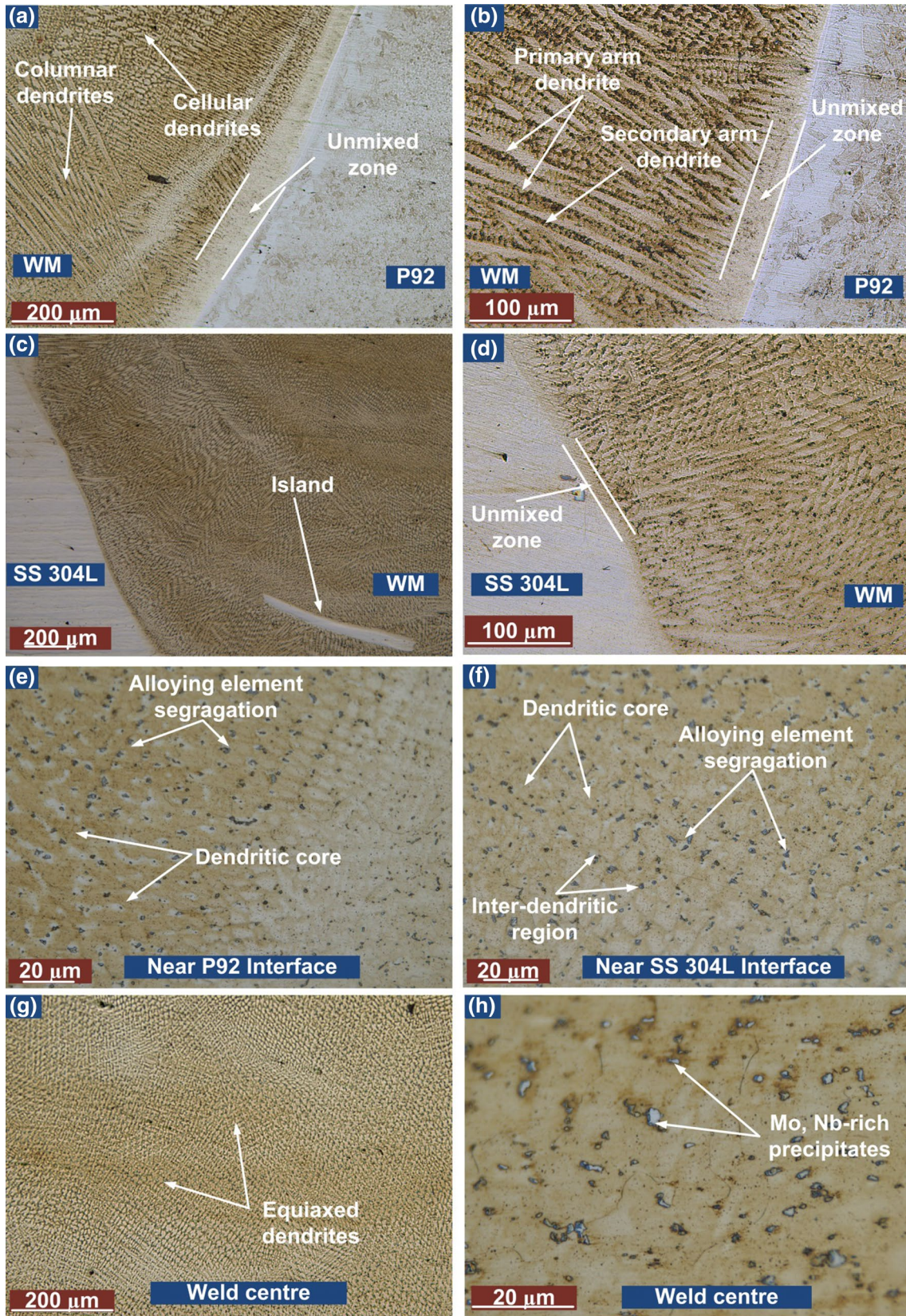




**Fig. 13** OM image of ERNiCrMo-3 weld fusion zone microstructure **a** unmixed zone toward P92 side, **b** formation of the secondary arm dendrites, **c** unmixed zone in the form of the island, **d** unmixed zone toward 304L SS side, **e** formation of the dendritic and inter-dendritic region toward P92 side, **f** formation of the dendritic and inter-dendritic region toward 304L SS side, **g** microstructure corresponding to the weld centre, **h** formation of the secondary phases at weld centre

different amount of the Cr, Ni, and Fe elements compared to the bulk weld metal and adjacent base metal. The dissimilar joining of the two different grades of steel using nickel-based filler always results in the formation of the unmixed zone at the weld interface due to the difference in chemical composition and melting temperature of the two materials. In addition, the diffusion of the elements occurs from the base metal to the weld metal and vice-versa. Thus, line mapping and electron probe microanalysis (EPMA) was performed across the weld interface to identify the elements movement across the weld interface. The line mapping and EPMA analysis, as shown in Figs. 16 and 17 confirm the significant variation of the various elements like chromium (Cr), nickel (Ni), and iron (Fe) at the unmixed zone. The EDS point analysis at the unmixed zone formed at the 304L SS and ERNiCrMo-3 weld fusion zone is shown in Fig. 18. The line mapping and EPMA analysis across the unmixed zone formed at the 304L SS and ERNiCrMo-3 weld fusion zone is shown in Figs. 19 and 20, respectively. Based on the EPMA analysis, the diffusion of the Cr, Ni, and Fe was observed, as displayed in Fig. 20.

The EPMA elemental mapping of the inter-dendritic region of the ERNiCr-3 WFZ is illustrated in Fig. 21. The Nb, Mo, Ti, and Cr spot is visible from the EPMA result. The Nb strongly tends to re-distribution in inter-dendritic regions during solidification due to its minimum equilibrium distribution co-efficient value ( $k < 1$ ). The formation of the secondary precipitates (tiny shining white particles) was observed from SEM images. The area mapping analysis in the SEM, as shown in Fig. 22 also revealed the segregation of the molybdenum (Mo), niobium (Nb), and titanium (Ti) particles in the inter-dendritic region of the weld fusion zone. The segregation of the Mo and Nb will form Mo and Nb depleted dendrite core in the weld fusion zone. Thus, the mechanical property and corrosion resistance provided by these elements will be affected in this region. Banovic et al. [11] also reported that elements such as Mo and Nb show a higher tendency of segregation due to their low equilibrium distribution co-efficient value ( $k$ ). It ( $k$ ) can be defined as the ratio of the solidus to liquidus concentrations for particular elements at a particular temperature. They also found the  $k$  value at different conditions. The value of  $k$  more than unity indicates that no dendritic micro-segregation will occur, but the value of  $k$  less than unity shows the opposite

behavior [41]. The  $k$  value for the Mo and Nb in Inconel 625 is between 0.75–0.86 ( $< 1$ ) and 0.3–0.45 ( $< 1$ ), respectively. Thus, it shows a higher tendency to segregate. The elements like Fe, Ni, and Cr show less tendencies to segregate due to its  $k$  value being higher than unity ( $> 1$ ). Also, they reported that Fe addition in nickel-based alloy decreases the segregation potential ( $k$ ) value for the Mo and Nb. Thus, the high Mo and Nb contents fillers are preferred for the welding of the dissimilar alloy to compensate for the Mo and Nb segregation. The formation of the Nb-rich eutectic secondary phases deteriorates the corrosion resistance and mechanical properties of the nickel-based weld. The weight percentage of the Mo and Nb in the chemical composition of the IN 625 filler is 9.23% and 3.96%, respectively. The Mo and Nb segregate during the solidification of the weld metal. The EDS point analysis was performed at these regions to obtain the approximate weight percentage of the Mo and Nb segregation. The EDS analysis showed ~17% of Nb and ~10% Mo in the weld metal. The results of the EDS analysis are shown in Fig. 23. However, the formation of the Nb-rich phase is undesirable as it has detrimental effects on the properties like toughness, creep, and ductility due to the consumption of a significant amount of useful alloying elements. The possible secondary phases (shiny precipitates) can be either Niobium carbide (NbC) or Molybdenum carbide ( $\text{Mo}_6\text{C}$ ), or Titanium Carbide (TiC). Also, Nb and Ti together can form (Nb,Ti)C [42]. The precise details can be obtained with the help of selective area electron diffraction (SAED) in transmission electron microscopy (TEM). This analysis falls outside the scope of present research work and is left for future scope.

### 3.4 Micro-hardness test

The micro-hardness variation across the base metal, weld fusion zone, and heat-affected zone in as-welded conditions and PWHT conditions are shown in Fig. 24a, b. The weld center was taken as the reference,  $x=0$ . The hardness value was measured along the longitudinal as well as the transverse direction of the weld center. The non-uniform profile of the micro-hardness distribution confirms the heterogeneity of the microstructure. The hardness of the 304L SS base metal was found to be lower than the P92 base metal and ERNiCrMo-3 weld metal. Thus, 304L SS base metal can be identified as a weaker region in P92/304L SS dissimilar weldments. The as-received P92 BM and 304L SS BM's micro-hardness values were  $230 \pm 10$  HV and  $170 \pm 10$  HV, respectively. According to the ASTM standard designation, A335/A335M-15a hardness of the P92 metal should not exceed 265 HV. The hardness beyond 265 HV indicates

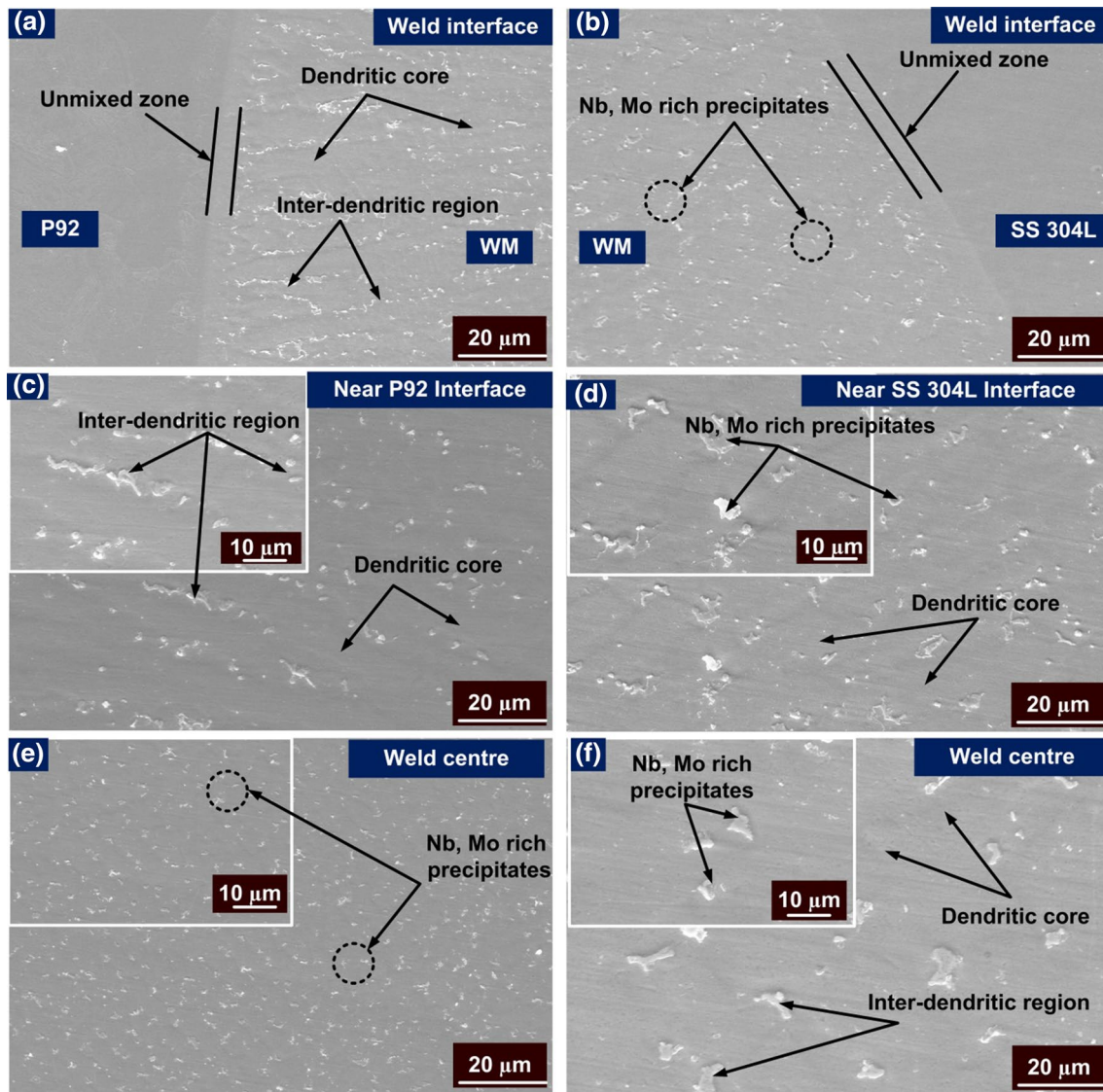


**Fig. 14** SEM image of ERNiCrMo-3 weld fusion zone microstructure **a** unmixed zone toward P92 side, **b** unmixed zone toward 304L SS side, **c**, **d** microstructure near the P92 and 304L interface, **e**, **f** forma-

tion of the dendritic and inter-dendritic region, and secondary phases at the weld centre

the brittle martensitic structure of the P92 steel, and it may result in the brittle failure of the components under the service. In the as-weld state, a sharp increase in hardness magnitude from the weld fusion zone to the P92 HAZ region with a sharp decrease in the ICHAZ region has been observed. In as-weld condition, P92 CGHAZ has the highest hardness value of the magnitude  $\sim 340$  HV. The high hardness value is due to the coarse prior austenite grains, untempered lath martensite structures and high weight percentage of C and N due to the dissolution of precipitates. The hardness value decreases as the distance from the fusion line increases. The hardness value of the FGHAZ was recorded as  $\sim 270$  HV. The low hardness value of the FGHAZ compared to the CGHAZ was due to the partial dissolution of

the precipitates. Next to the FGHAZ, the soft region with the very low hardness value was observed, which is called ICHAZ. The ICHAZ region has the lowest hardness value of the magnitude  $\sim 205$  HV. The low magnitude is due to the formation of the combinations of ferrite and newly formed martensite structures. Thus, hardness distribution along the P92 HAZ confirms the presence of three distinguished zone. The hardness value of the CGHAZ and FGHAZ was decreased after PWHT because of the tempering of the fresh martensite formed during the welding and the precipitation of the  $M_{23}C_6$  and MX precipitates. The hardness value of the CGHAZ and FGHAZ was reported as  $\sim 235$  HV and  $\sim 210$  HV, respectively, after PWHT. After PWHT, ICHAZ was still the region with the lowest microhardness value. After

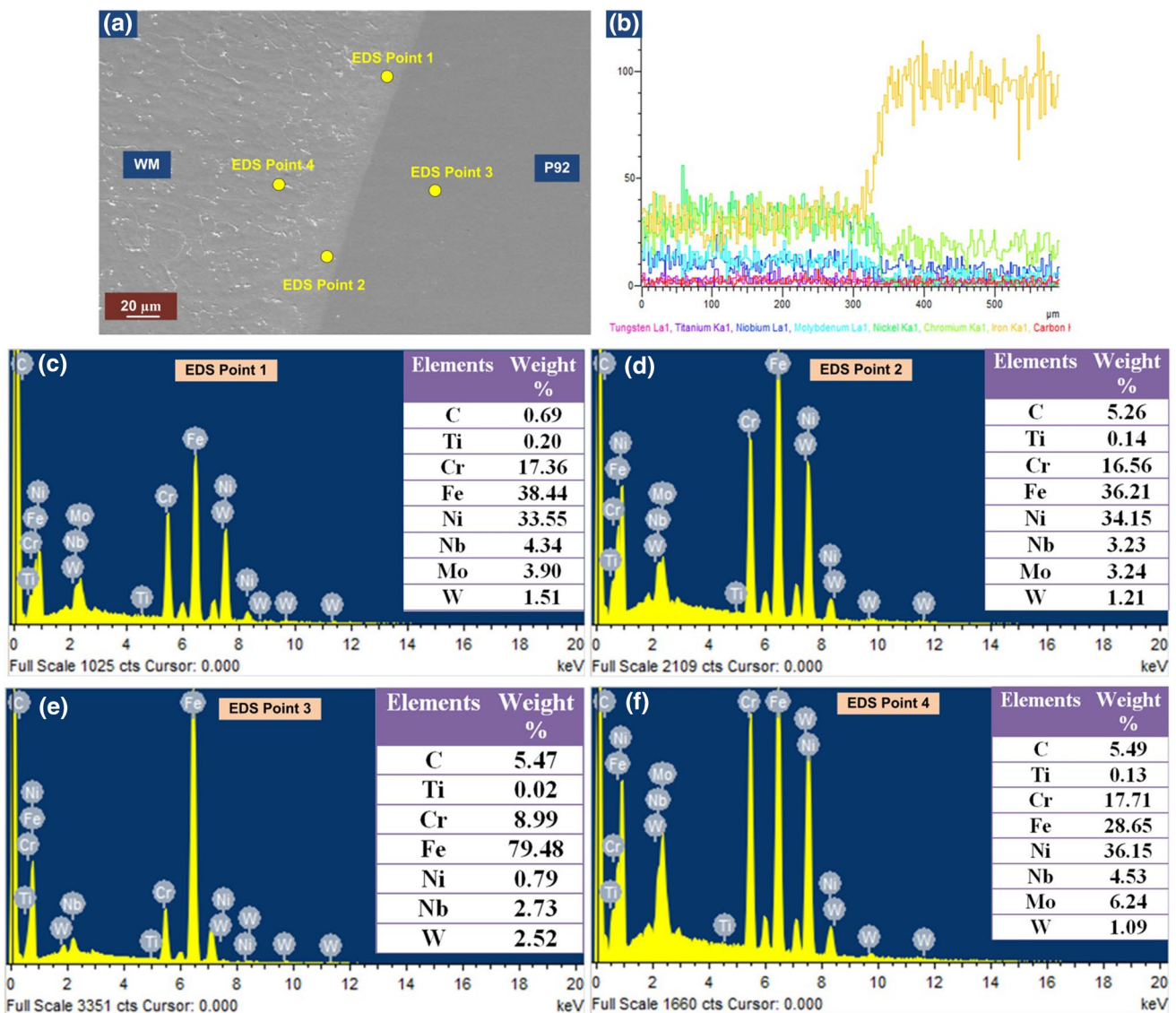


**Fig. 15** a EDS analysis location across P92 and WM, b Line map across the P92 and WM, c EDS result of point 1, d EDS result of point 2, e EDS result of point 3 f EDS result of point 4

PWHT, due to re-precipitation of the dissolved precipitates and coarsening of the existing precipitates, the hardness of the ICHAZ region was recorded as ~200 HV. The partial austenitization, coarsening, and dissolution of precipitates led to the low dislocation density from the complex microstructure of the ICHAZ region. This complex microstructure, as shown in the previous section, is most susceptible to type IV cracking. This soft zone (ICHAZ) is a very critical region and may be responsible for premature Type IV cracking in power plant components during service conditions [39]. The region next to the ICHAZ is over-tempered base metal. This region does not undergo any partial austenite ↔ martensite transformation like ICHAZ. This over-tempered region has a hardness lower than the base metal due to

the additional tempering that occurred during welding. Thus it can be assumed that this region has very limited microstructural change. In addition, this over-tempered region has a very limited span, as shown in the microhardness profile. This region gets disappears as the distance from the fusion line increases. The hardness of the fusion zone in as-weld condition was  $200 \pm 15$  HV, while the hardness of the fusion zone after PWHT was  $210 \pm 25$  HV. This variation in the hardness value of the ERNiCrMo-3 weld fusion zone may be due to the diverse microstructure (like columnar, cellular, and equiaxed dendritic and formation of secondary phase) of the weld fusion zone formed due to the variation in the cooling rate from the weld center to the fusion boundary. The PWHT at 760 °C, 2 h was conducted to modify the

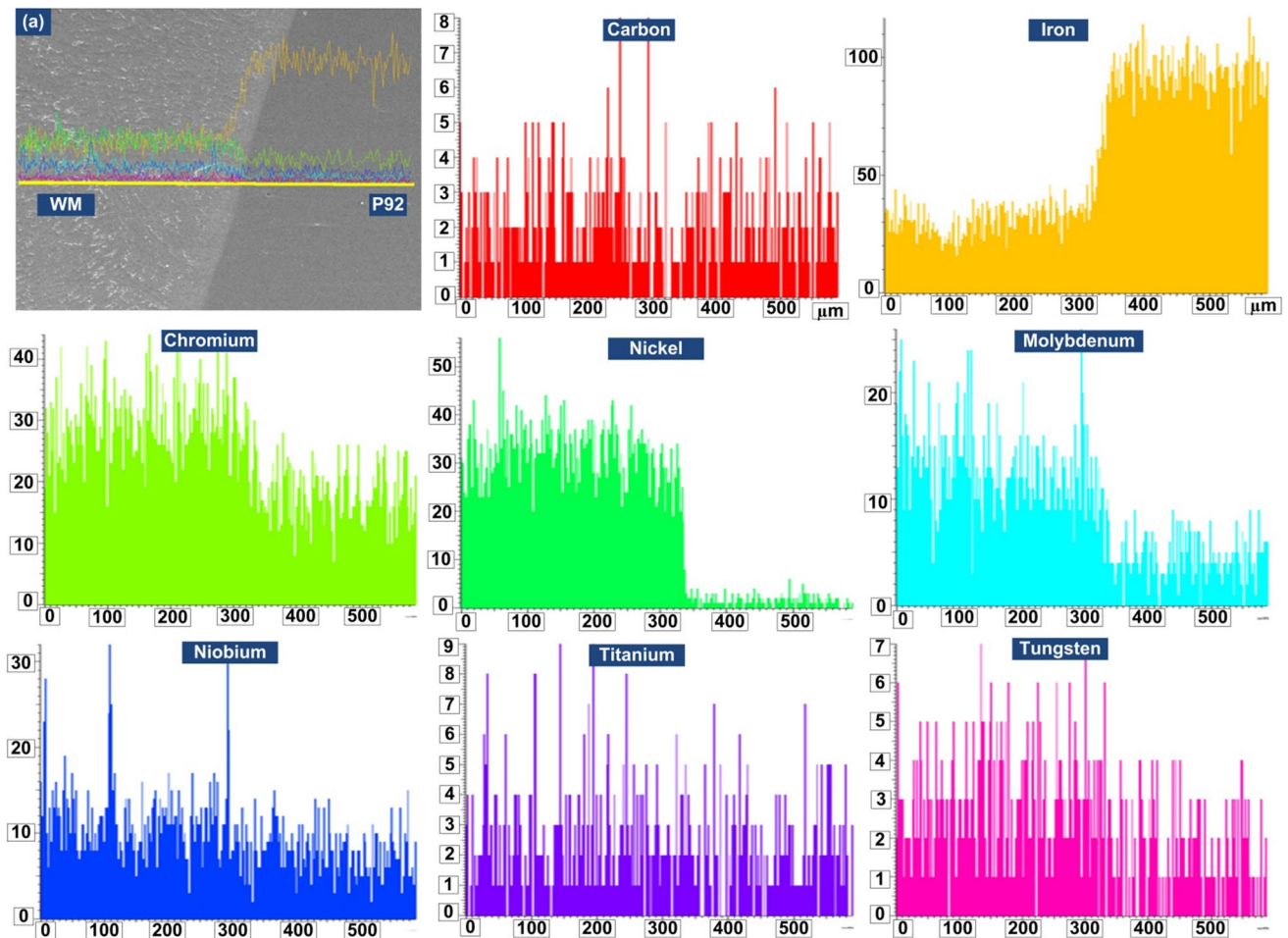


Fig. 16 Line mapping across the ERNiCrMo-3 weld metal and P92 base metal

microstructure of the P92 HAZ. However, a slight increase in hardness and toughness properties was also noticed for the ERNiCrMo-3 weld fusion zone after PWHT. Thus, it can be expected that PWHT at 760 °C, 2 h somewhat alters the size and characteristics of the precipitates present in the weld fusion zone. The approximate hardness value toward the 304L SS side was  $170 \pm 10$  HV in as-welded and PWHT conditions. The PWHT for 2 h at the temperature of 760 °C is the optimum parameter suggested by various researchers based on the outcome of the mechanical and microstructural properties [43]. The welding heat resulted in the dissolution of the precipitates and the formation of quenched martensite microstructure. This microstructure is brittle in nature and thus, PWHT known as tempering was performed for the re-precipitation of the precipitates and to get a tempered martensite microstructure. The PWHT for 2 h at the temperature of 760 °C results in the formation of the Cr-rich precipitate in the microstructure of austenitic steel which contributes to the growth of hardness. However, this hardness change is insignificant as can be verified from the micro-hardness

graph in the AW state and after PWHT. Thus, it can be concluded that welding and heat treatment do not alter the hardness of 304L SS metal. The micro-hardness variation along the root to the top of the weld fusion zone in as-weld state and after PWHT is shown in Fig. 24c, d, respectively. The multiple thermal cycles due to the multipass welding, and simultaneous cooling and tempering effects cause this non-uniform micro-hardness distribution.

#### 4 Tensile test

The tensile test was performed on DWJs prepared using ERNiCrMo-3 filler in as-welded and PWHT conditions. The specimens were prepared according to the ASTM E-08 standard. The tensile strength of the P92 and 304L SS base metal was observed as 758 MPa and 632 MPa, respectively. The UTS of the P92/304L SS DWJs in an as-weld state and after PWHT was 626 MPa and 562 MPa, respectively. It is evident from the test that the specimen fractured from the

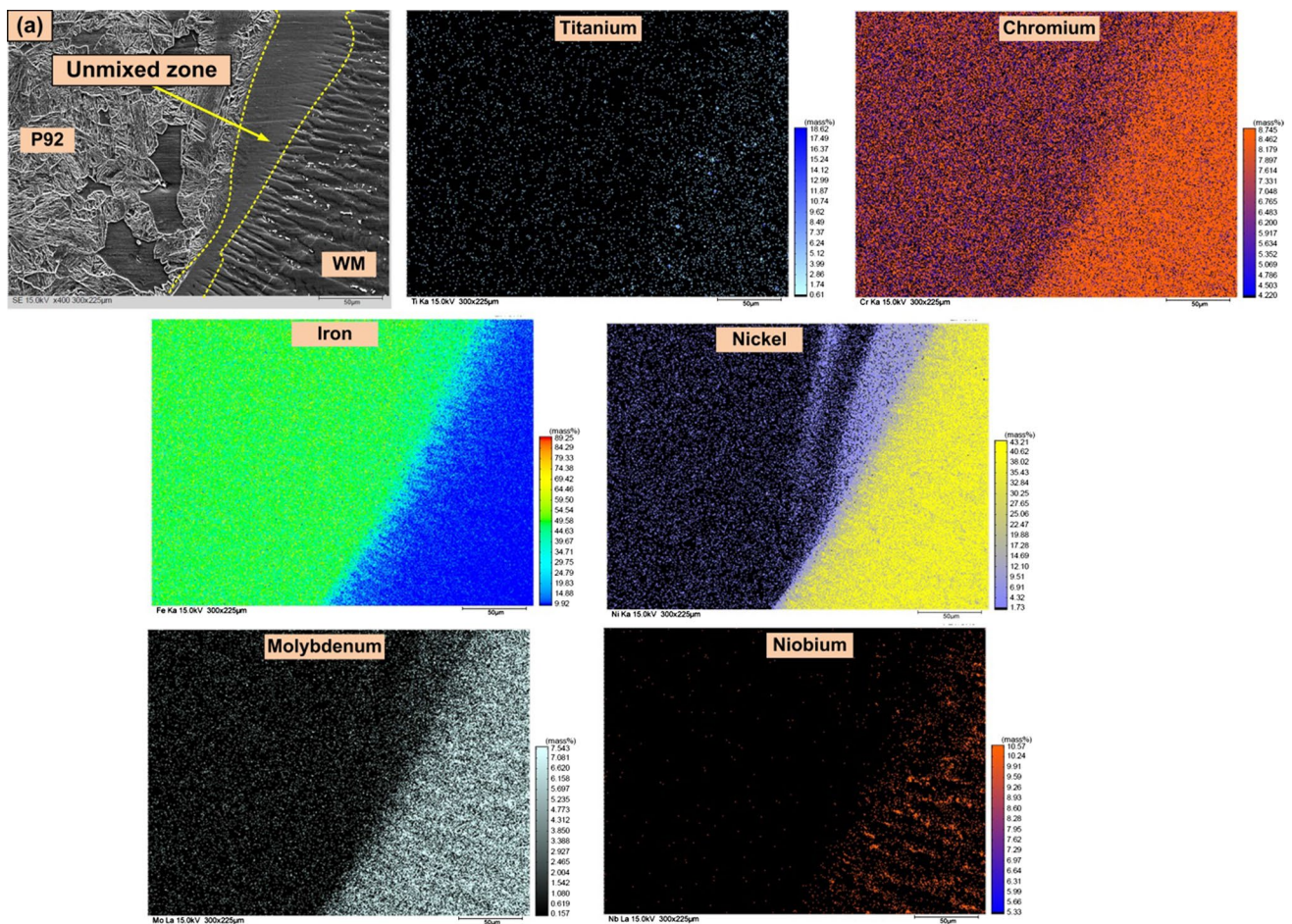


**Fig. 17** EMPA analysis across the P92 HAZ and ERNiCrMo-3 weld fusion zone interface

304L SS BM in both the condition, as shown in Fig. 25a. Thus, 304L SS was the weakest link in P92-ERNiCrMo-3-304L SS DWJs. Thus, it also confirms the micro-hardness results. The percentage elongation of the P92/304L SS weldments in as-welded and PWHT conditions was 41% and 56%, respectively. In PWHT conditions, the percentage elongation was more compared to the as-welded conditions due to the tempering of the quenched martensite formed during the welding. Thus, after PWHT, dissimilar weldments will take more time to fracture compared to the as-welded conditions. The P92 HAZ and ERNiCrMo-3 weld metal were safe in all conditions. The weld fusion zone undergoes small plastic deformation during the tension test, but it does not rupture. The stress–strain curve is shown in Fig. 25b. The fractured tensile specimens show the necking at the rupture location. The ultimate tensile strength, yield strength, and percentage elongation of the specimens tested in each condition are listed in Table 6. According to the ASME BPVC Section IX for the acceptance of tensile test results: “If the specimen

breaks in the base metal outside of the weld or weld interface, the test shall be accepted as meeting the requirements, provided the strength is not more than 5% below the minimum specified tensile strength of the base metal. Thus, according to this criterion, specimens were qualified for the tensile test. The minimum specified mechanical properties of the P92 steel and 304L SS are available in ASTM A335/A335M-15a and A240/A240M-04a standards. The fracture surface analysis of the tensile and Charpy test specimens was carried out using SEM to determine the fracture mode of the specimen. The fractograph obtained for the as-weld and after PWHT tensile test fracture specimen is shown in Fig. 26a–d. As shown in Fig. 26a, b, the fractograph of the as-weld tensile specimen consists of micro-voids, dimples and secondary phase particles on the fracture surface. The PWHT tensile specimen consists of tear ridges, less number and dimples on the fracture surface as shown in Fig. 26c, d. Thus, the fractograph confirms the ductile fracture of the tensile specimen.

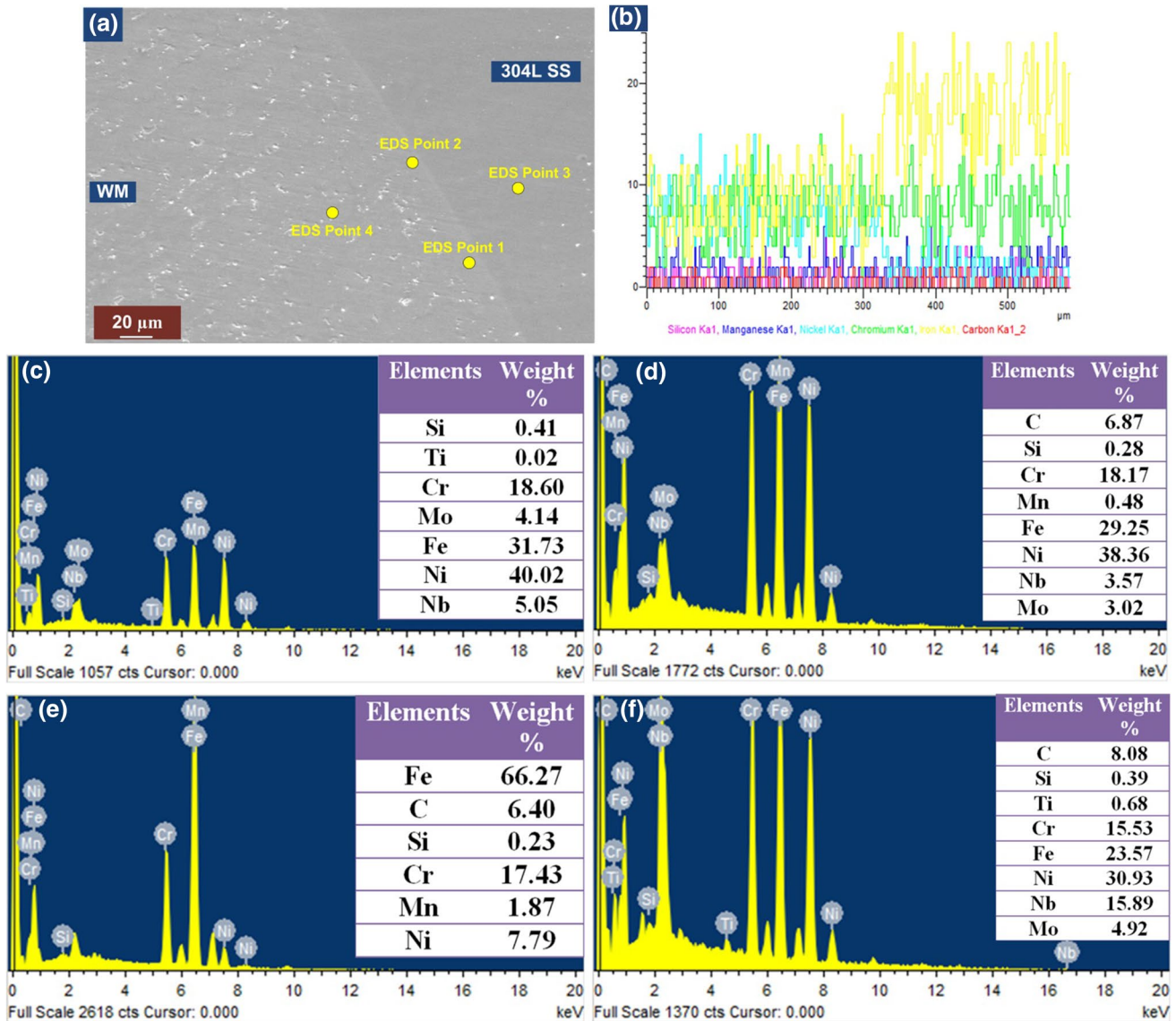


**Fig. 18** a EDS analysis location across 304L SS and WM, b Line map across the 304L SS and WM, c EDS result of point 1, d EDS result of point 2, e EDS result of point 3 f EDS result of point 4

### 4.1 Impact toughness test

The Charpy V-notch test was performed to ensure the ability of the welded joint to withstand sudden thermal impact shock. As shown in Fig. 27a–c, the V-notch was cut at the weld center, P92 HAZ, and 304L SS HAZ side. The surface of the specimens after the test is shown in Fig. 27d–f. The obtained impact toughness result is shown in Fig. 28, along with the impact toughness of 304L SS and P92 base metal. The average impact energy of the P92 BM and 304L SS BM is  $185 \pm 5$  J and  $285 \pm 5$  J, respectively. The high toughness of the 304L SS BM is due to the wrought and annealed austenitic grains. The impact energy of the ERNiCrMo-3 weld metal was the lowest compared to all other regions.

The impact strength of the weld metal was 57 J and 72 J, respectively, in as-weld state and after PWHT. The results revealed that the region with relatively poor impact toughness was austenitic ERNiCrMo-3 filler weld (57 J) because of the segregation of the Nb and Mo along the inter-dendritic areas. However, the impact toughness of ERNiCrMo-3 filler weld met the minimum requirement of 47 J (EN ISO 3580:2017). Thus, the toughness of the weld joint is qualified for USC application. The low toughness of the weld metal is due to the higher segregation of the Mo and Nb-rich secondary phases as already discussed in the previous section and shown in Fig. 14f. It has been reported that coarse dendrites in the weld metal (fewer grain boundaries) result in a low impact toughness of the joint. The grain growth

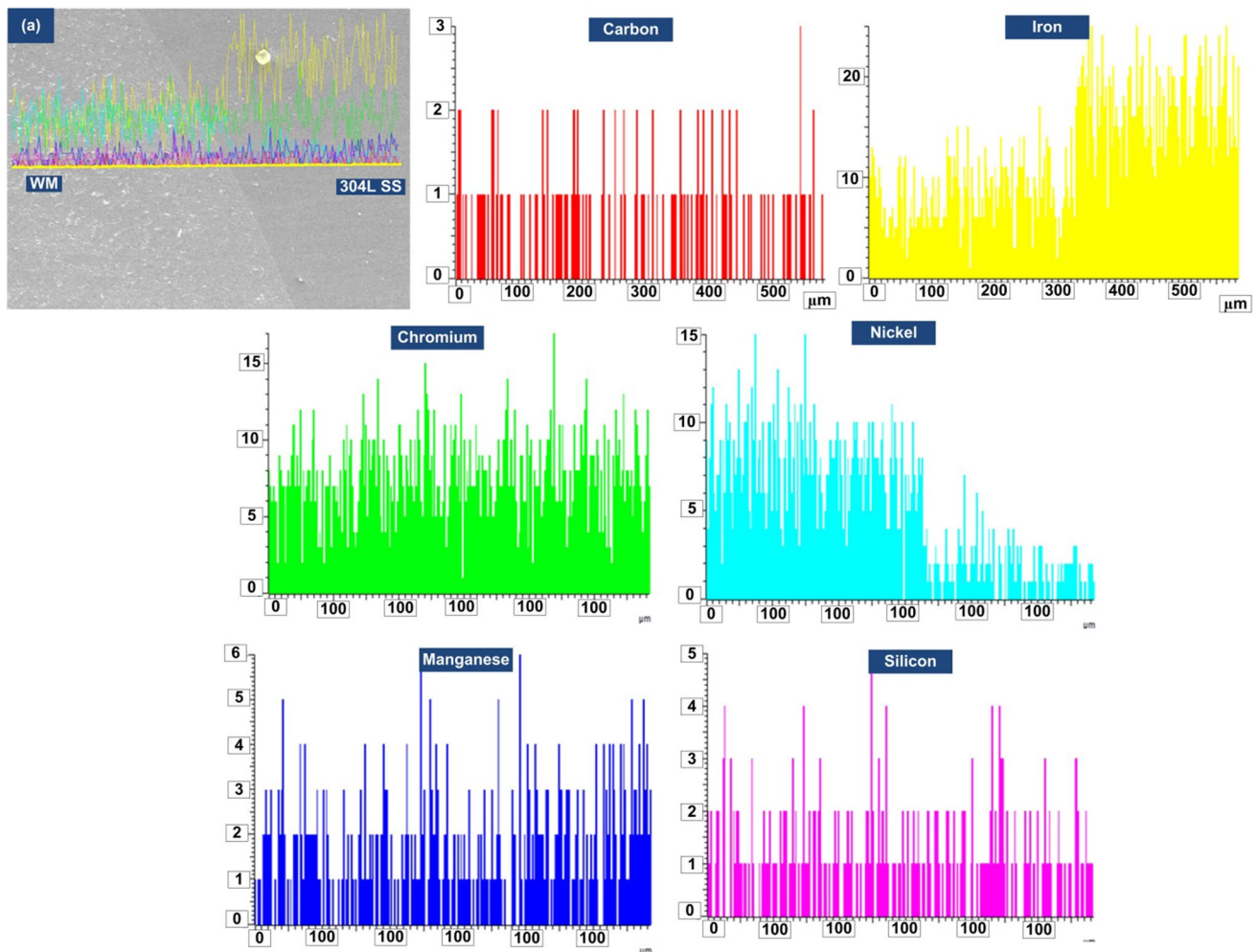


**Fig. 19** Line mapping across the ERNiCrMo-3 weld metal and 304L SS base metal

and change in orientation factor during the welding results in the reduction in impact strength of that particular location [10]. For weld metal during welding, the orientation is formed in a transverse direction. In this situation, a crack is easily formed and propagates, thus lowering the weld joint's impact strength. The ERNiCrMo-3 weld metal exhibits a brittle mode of fracture. Ramkumar et al. [44] also observed the low impact toughness of the ERNiCrMo-4 (61 J) and ERNiCrMo-10 (67 J) weld fusion zone during the Inconel 625 and Inconel 718 dissimilar welding. They reported that the formation of secondary phases due to the segregation of the Mo, Nb, and Ti deteriorates the impact strength of the fusion zone. The impact strength of the P92 HAZ was 149 J and 163 J in the as-welded state and PWHT, respectively. The toughness of the P92 HAZ in as-weld and PWHT conditions was lower than the P92 BM. The low impact toughness is due to the coarse grains compared to the P92 BM. The impact strength of the 304L SS HAZ was 280 J and 253 J, respectively, in as-weld and PWHT conditions. The impact

strength of the 304L SS HAZ was lower than 304L SS BM after PWHT due to the coarsening of the austenite grains. For the V-notch at P92 and 304L SS HAZ, all specimens demonstrated ductile fracture mode in as-weld and PWHT condition. The fractograph obtained for the ERNiCrMo-3 weld metal of as-weld and after the PWHT Charpy test fracture specimen is shown in Fig. 29a–d. As shown in Fig. 29a, b, the fractograph of the as-weld Charpy impact test specimen consists of dimples on the top surface. It also consists of secondary phase particles on the fracture surface. The as-weld specimen shows the mixed mode of fracture. The PWHT Charpy test specimen also shows a mixed mode of fracture as shown in Fig. 29c, d.

## 4.2 Residual stress analysis

The DHD technique is the most accurate experimental method available for measuring the welding-induced residual stresses. The through-thickness residual stress

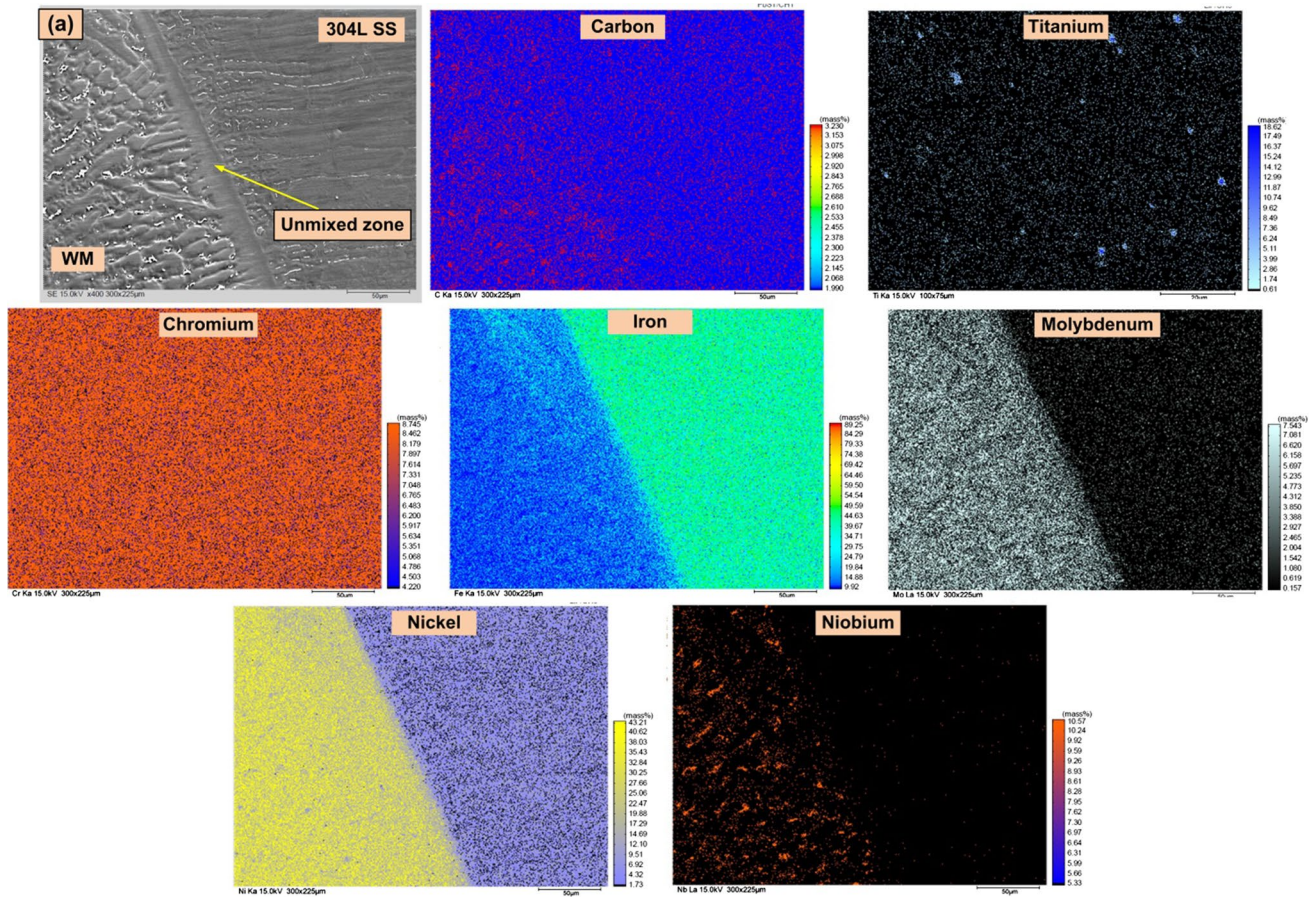


**Fig. 20** EMPA analysis across the 304L SS and ERNiCrMo-3 weld fusion zone interface

distribution in as-weld and PWHT (760 °C, 2 h) condition for the ERNiCrMo-3 weld fusion zone, P92 steel HAZ, and AISI 304L SS HAZ is shown in Fig. 30a–c. The peak longitudinal residual stress of magnitude 269 MPa was observed at a depth of 3 mm for the weld fusion zone. The longitudinal residual stress of tensile nature was observed throughout the weld. The transverse residual stress of tensile nature was observed up to 5 mm depth, and later it converted into a compressive nature. The high tensile residual stress in the weld fusion zone is due to the shrinkage during the weld solidification. The tensile residual stresses are more detrimental as they are responsible for the weld's stress corrosion cracking, fracture, and fatigue damage [45]. For the ERNiCrMo-3 weld zone in the as-welded condition, the maximum transverse tensile residual stress observed was 101 MPa. After PWHT, the longitudinal residual stress of tensile nature was observed up to 5 mm thickness, and later it converted into a compressive nature. After PWHT, peak longitudinal stress magnitude reduced from 269 to 49 MPa. Thus, PWHT lessens the residual stresses to a great extent. In addition, due to the multipass welding, the tempering effect takes place after

each pass. This tempering effect also relaxes the residual stresses. The longitudinal and transverse residual stress magnitude was less due to the less weld metal available for the solidification of the narrow groove geometry. Taraphdar et al. [23] also concluded that narrow groove geometry is beneficial in reducing the peak longitudinal residual stresses in the weld zone.

For P92 HAZ, the stress observed was compressive due to the volume change during the phase transformation. Li et al. [46] also reported a similar kind of observation. They reported that the yield strength of the P92 steel decreased during the phase transformation from the tempered martensite to the austenite during welding. After welding is completed (during cooling), the yield strength increases during the phase transformation from the austenite to the untempered martensite, this yield strength variation caused due to the phase transformation induces the plasticity in the P92 steel. After welding, the P92 steel undergoes the solid-state phase transformation (SSPT) during rapid cooling (austenite to martensite transformation). The P92 steel contract during the austenitization process ( $Ac_1$  to  $Ac_3$ ), and then it expands from the martensite start temperature ( $M_s$ ,



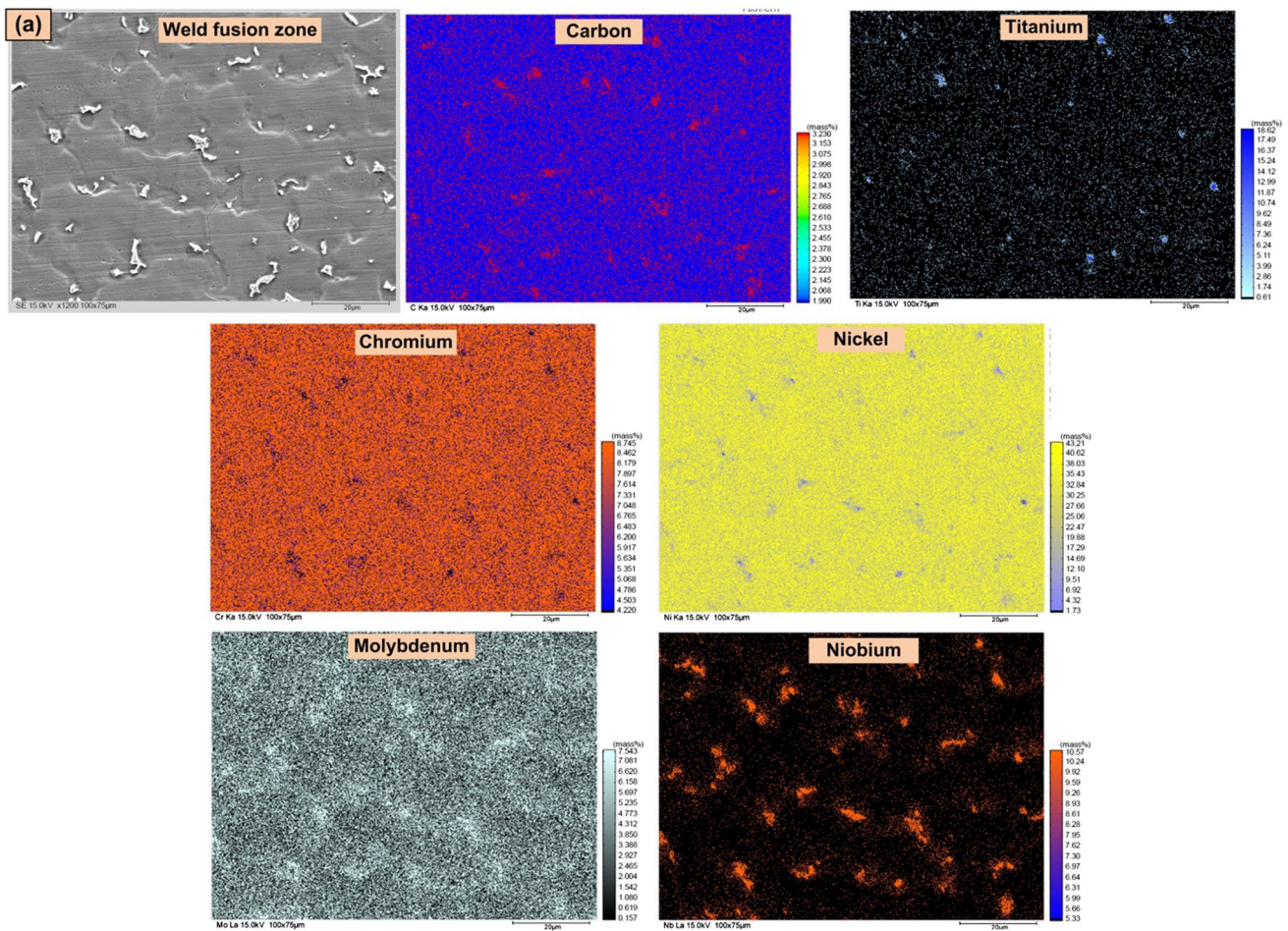


**Fig. 21** EMPA analysis across the ERNiCrMo-3 weld fusion zone

375 °C) to the martensite finish temperature ( $M_f$ , 280 °C). During the austenitization process, steel changes its crystal structure from body-centred cubic (BCC) to FCC. Then, it changes from face-centred cubic structure (FCC, Austenite) to body-centred tetragonal structure (BCT, Martensite) during  $M_s$  to  $M_f$  [47]. This phase change results in the volumetric change into the P92 steel and induces the plasticity known as transformation-induced plasticity (TRIP) [48]. This phenomenon changes the yield strength and the nature of the residual stresses from longitudinal to compressive and vice versa. The tensile residual stress was developed in the weld fusion zone due to the shrinkage during the weld metal solidification, while compressive stress was developed in P92 HAZ due to the volume expansion during martensite transformation [49]. The high residual stresses present in the HAZ of the P92 steel may lead to the premature failure of the DWJs from the HAZ of the P92 steel. Thus, the accurate measurement of the residual stresses linked with the P92 HAZ is essential considering the effect of the SSPT and yield strength variation associated with the P92 steel. From

the residual stress magnitude listed in Table 7 for 304L SS HAZ, it can be concluded that the stresses in HAZ of 304L steel exceed the yield stress of this material. However, the residual stress exceeds the yield stress of the material within the interior of the metal. Within the interior the residual stresses can be tri-axial so they can greatly exceed the uniaxial yield stress measured in a tensile test. Thus, it is a little unfair to compare both value. As in the present case the stress was measured for through thickness (within the interior of the metal) using a deep hole drilling technique. For the 304L SS HAZ, the maximum transverse tensile residual stress observed was 169 MPa. Also, after PWHT, the maximum transverse tensile residual stress observed for narrow groove design was 71 MPa. The mismatch in the coefficient of the thermal expansion between the P92 steel and 304L SS results in the non-uniform residual stress distribution. When residual stresses are very high the material becomes poor in tensile strength. The failure of the tensile test samples from the 304L SS material indicates the influence of

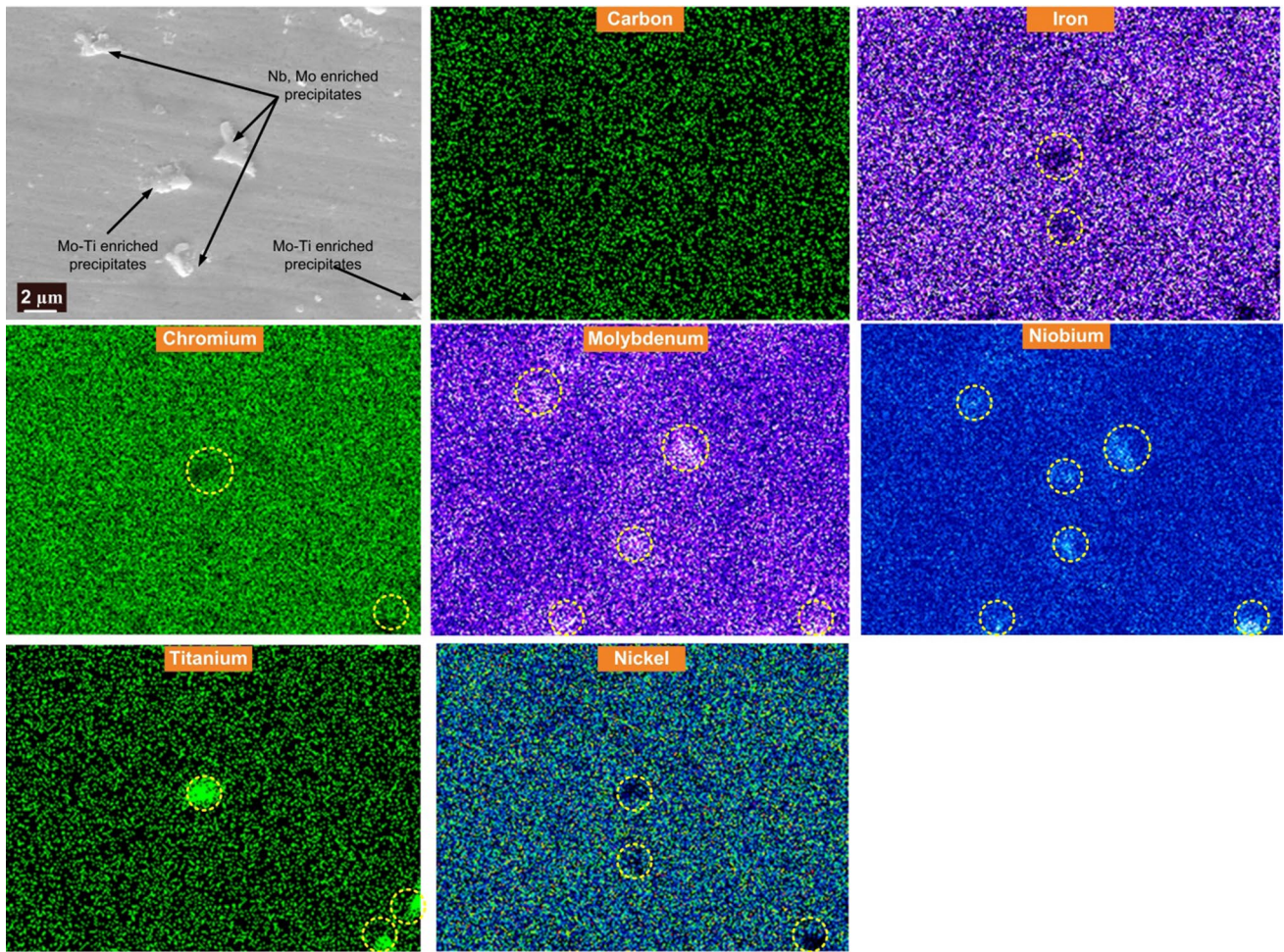


Fig. 22 Segregation of the Mo, Nb and Ti elements

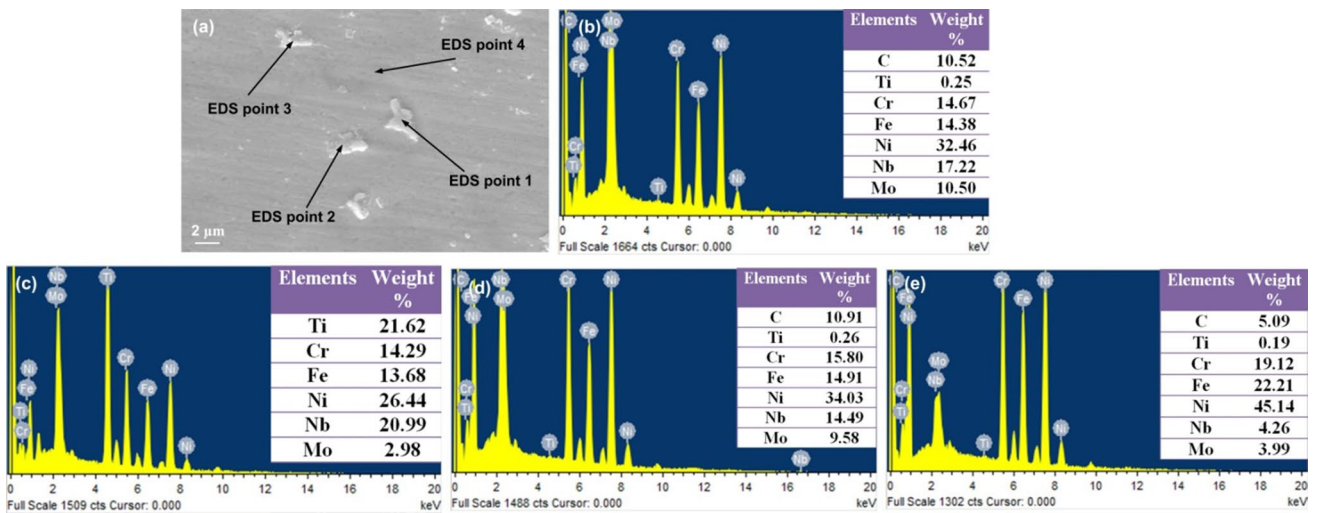
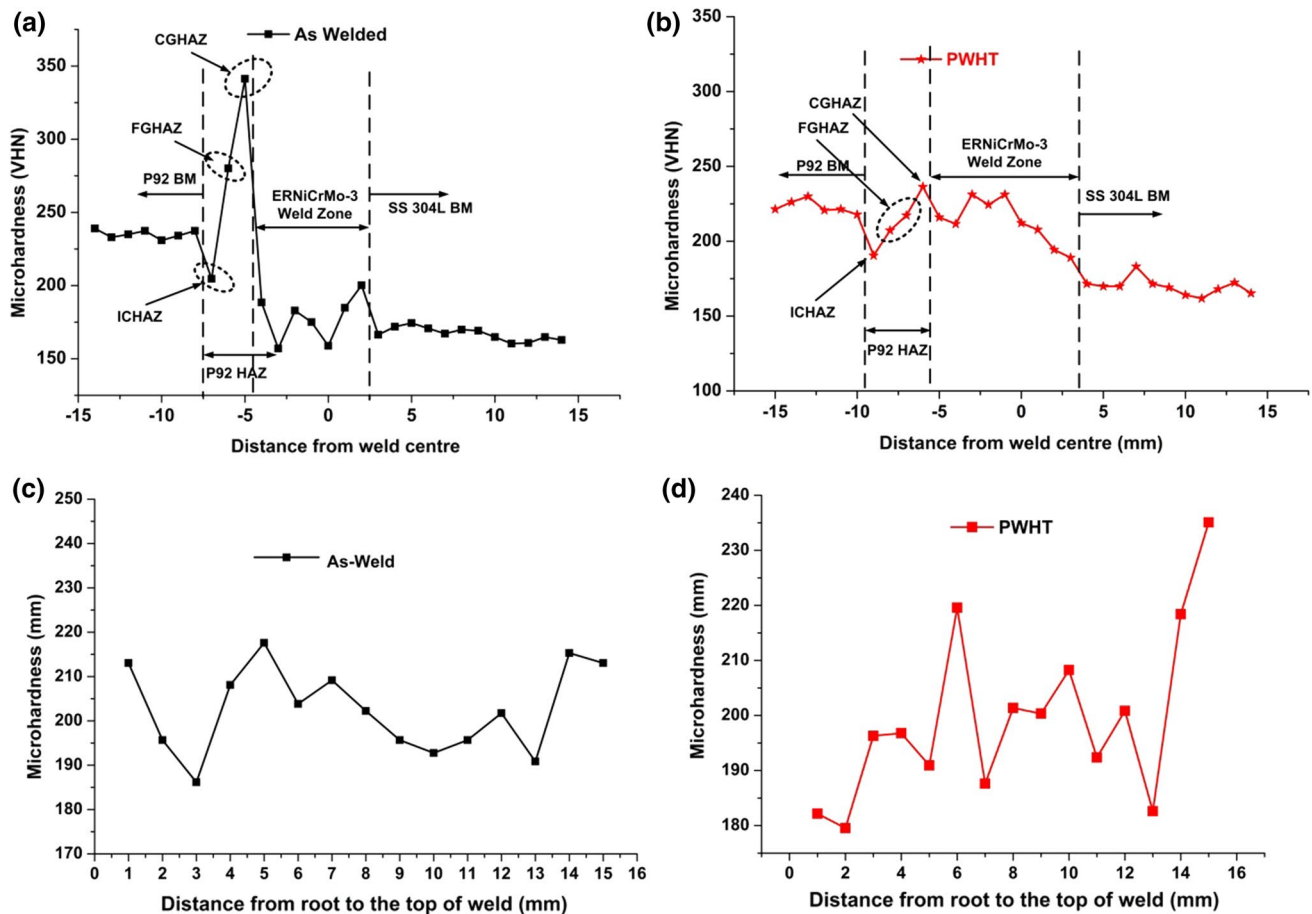


Fig. 23 a SEM image of the secondary phase, b–d EDS point analysis results of the location 1, 2, 3 and 4, showing the segregation of the Nb, Mo and Ti elements



**Fig. 24** a, b Micro-hardness distribution across P92 and 304L SS DWJ in as-weld state and after PWHT, c, d Micro-hardness distribution across ERNiCrMo-3 weld zone from root to the top in as-weld state and after PWHT

the high residual stresses on the mechanical properties of 304L SS metal.

## 5 Discussion

The CSEF P92 steel was welded with 304L ASS. The dissimilar joining of these two different grades of material was performed using the TIG welding process. The nickel-based ERNiCrMo-3 (Inconel 625) welding consumable was used. The mechanical properties, microstructural characteristics, and residual stresses of DWJs were examined. The influence of PWHT (760 °C, 2 h), called as tempering, was also investigated. The radiographic examination and macrostructure analysis showed defect-free P92/304L SS DWJs. The macrostructure showed the full depth and width of penetration. The DWJ was free from macroscopic defects, as confirmed by the macrograph. The clear HAZ formation toward the P92 side was observed from the macrograph. The insignificant

HAZ was observed near the 304L SS side as a result of low thermal conductivity. The specimens were prepared for the mechanical and microstructural examination after ensuring the defect-free weld joint using x-ray radiographic examination and macrostructure analysis. The various zone formed on either side of the fusion boundaries and ERNiCrMo-3 weld metal were investigated for microstructure evolution using an optical and scanning electron microscope. Due to the partial melting of the P92 HAZ during the welding, various metallurgical changes occur in the P92 HAZ region. The different peak temperatures experienced by the P92 HAZ during the weld thermal cycle result in the formation of CGHAZ, FGHAZ, and ICHAZ. At a temperature above 1500 °C, the metal is entirely in a liquid state. Below 1500 °C, when it starts to solidify, the coarse prior austenite grains (grain growth zone) and fine delta ferrite grain form. The CGHAZ is formed at a temperature much above the upper critical temperature ( $A_{c3}$ ). This temperature is

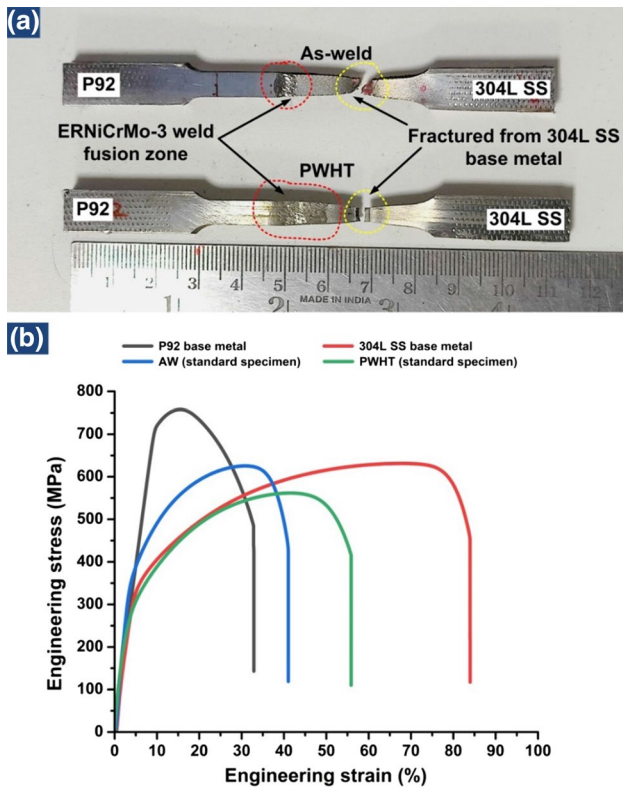


Fig. 25 a Tensile specimen after fracture and b stress–strain curve

sufficient to cause the dissolution of the precipitates. Thus, precipitates are unable to restrict the movement of grain boundaries. This allows the austenitic grain to grow bigger in size and thus forming CGHAZ. The delta ferrite ( $\delta$ -Fe) is formed during the solidification of the P92 steel. This delta ferrite phase will then transform into the austenite phase ( $\gamma$ -Fe) during cooling. However, it is possible that due to rapid cooling a small amount of a  $\delta$ -Fe does not transform into austenite. The part of this austenite phase may again transform into the alpha ferrite phase ( $\alpha$ -Fe) at a low temperature. This alpha ferrite is very soft in nature, and thus it caused low micro-hardness of the ICHAZ region. The various phase transformation taking place in the P92 steel during cooling and heating can be better understood from the phase diagram of the P92 steel [50]. The microstructure formed in

the P92 HAZ after welding is highly brittle because of the development of the quenched martensite and the dissolution of precipitates. Thus, DWJs must undergo PWHT (tempering heat treatment) to obtain desired microstructural and mechanical properties. The secondary electron and optical image confirmed that ERNiCrMo-3 weld metal is accompanied by an equiaxed austenitic microstructure with a high Ni weight percentage. The SEM area mapping analysis results of the weld fusion zone revealed the Nb, Cr, and Ti segregation in the inter-dendritic region. During the room temperature tensile test, the AW and PWHT specimens failed from the low UTS material, i.e., from the 304L SS base metal. The result of the tensile test also supports the result of the micro-hardness examination. From the residual stress measurement for the ERNiCrMo-3 weld fusion zone, it was observed that longitudinal residual stresses were higher than the transverse residual stresses. It was observed that residual stress was high at the top layer of the weld, and it was gradually reduced from mid-section to the root of the weld. The residual stresses are generated due to the volumetric expansion and contraction of the weld metal. The high volume of the weld metal leads to high shrinkage, which is opposed by the base metal region. Thus, high tensile residual stresses are accumulated. The high volume of the weld metal at the top of the narrow shape groove weld design results in the high welding-induced residual stresses at the top surface of the weld. The less volume of the weld metal at the mid-section and root of the V-groove weld design results in less welding-induced residual stresses at the root and mid-section. For the P92 HAZ, compressive longitudinal and transverse residual stresses were observed in as-weld and PWHT situations. For P92 HAZ, the stress observed was compressive due to the volume change during the phase transformation. In AW and after the PWHT condition, a considerable difference in the residual stress magnitude was noticed. From comparing mechanical and microstructural properties obtained for narrow shape groove geometry DWJs, it was found that narrow groove design reduces the overall heat-affected zone span, and it also requires less welding time and less heat input due to the less weld deposition because of the low included angle in narrow groove geometry.

Table 6 Mechanical property of the weld joint

DWJ condition	Tensile strength (MPa)	0.2% yield strength	% elongation	Fracture location	Joint efficiency (%)
P92 BM	758	710.42	32.87	–	–
304L SS BM	632	209.12	83.96	–	–
As-welded	626	311.37	41.02	304L BM	99.104
PWHT	562	190.37	55.87	304L BM	88.98

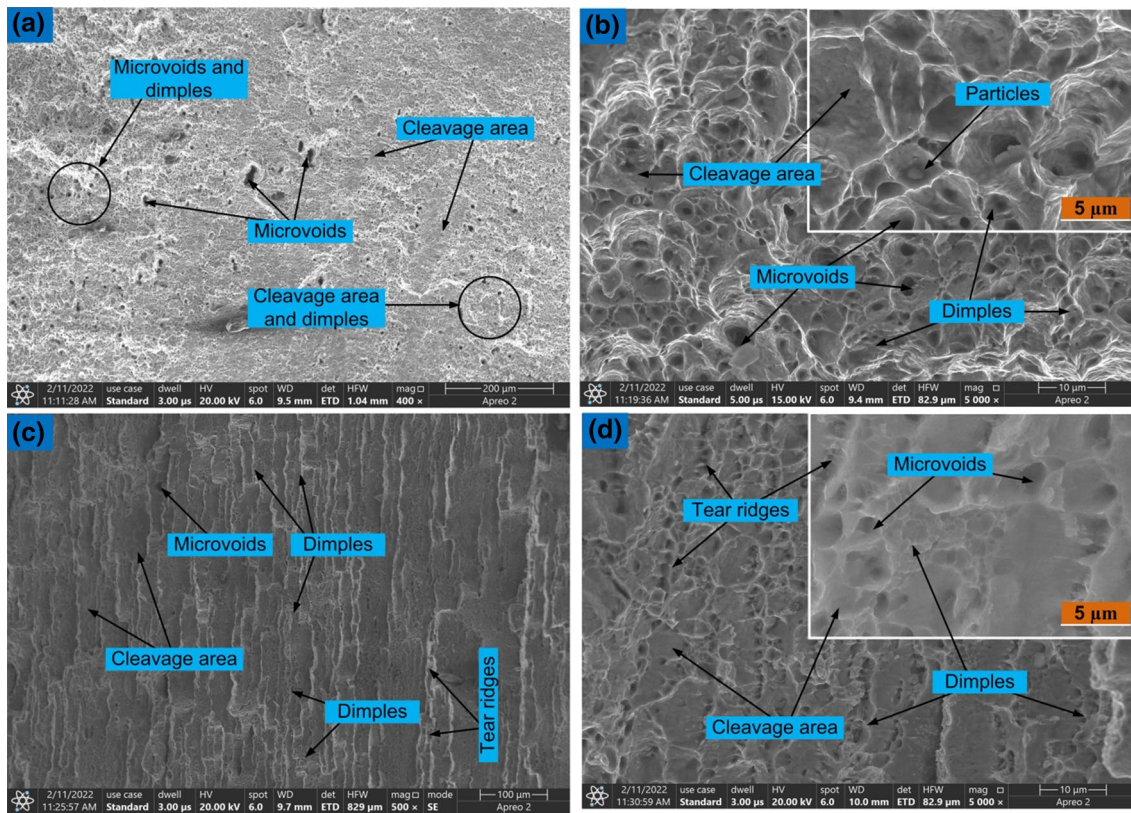


Fig. 26 Fractograph of the P92/304L SS DWJs (a, b) as-weld tensile test specimen and c, d PWHT tensile specimen

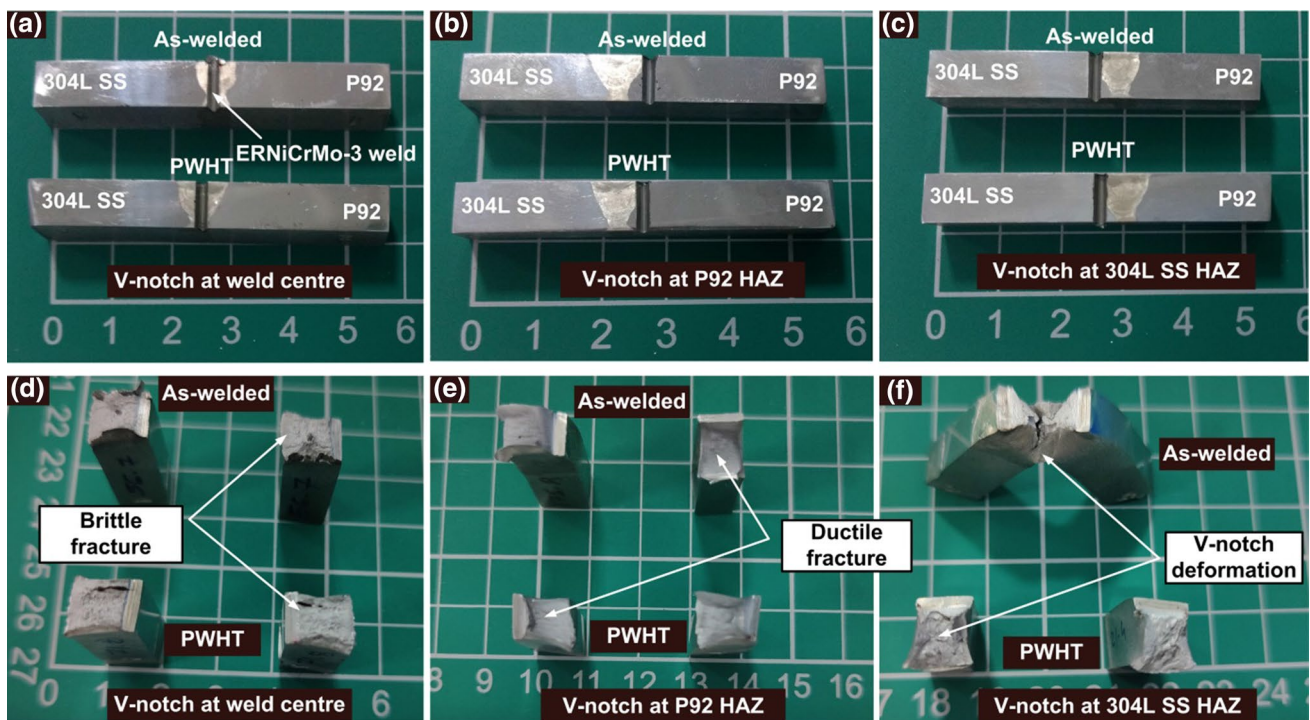


Fig. 27 a–c Charpy V-notch specimens in as-weld and PWHT conditions before test, d, e fracture surface of various specimens after test

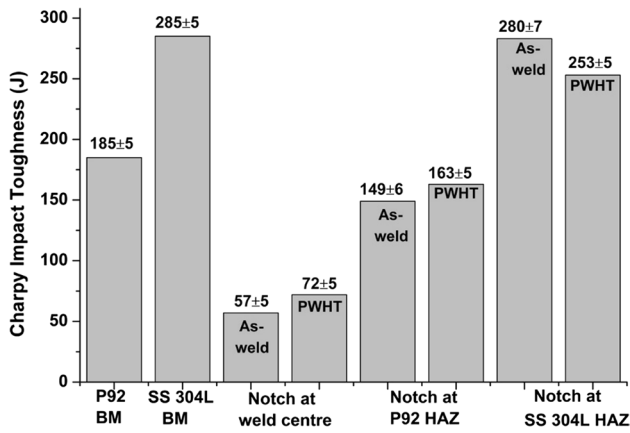


Fig. 28 Charpy V-notch test result

### 6 Conclusions

From the analysis of the microstructure characteristics, mechanical properties, and residual stresses of the P92 and 304L SS dissimilar welds in as-welded and PWHT conditions, it can be concluded that:

- (1) The welding parameters and the welding technique employed for narrow groove design accurately made defect-free weld joint.
- (2) Radiographic test and macrostructure show decent weld joint quality with no significant defect and good base and filler metal fusion. The weld and HAZ region was free from the solidification cracking and liquation cracking, respectively.
- (3) The steep micro-hardness gradient was observed within the P92 HAZ region after welding. This steep hardness profile confirms the heterogeneous microstructure formed within the P92 HAZ region after welding. The PWHT at 760 °C, 2 h stabilizes the microstructure and makes the hardness profile stable.
- (4) The ultimate tensile strength of the P92-ERNiCrMo-3-AISI 304L SS dissimilar joint was 626 MPa and 562 MPa, respectively, in as-weld and PWHT conditions. The UTS value was decreased and elongation was increased after PWHT due to the tempering of the quenched martensite formed during welding. The specimens failed from the 304L SS base metal in both conditions. The obtained strength value satisfies the minimum required strength criteria.
- (5) The impact energy of 57 J and 72 J was recorded for the weld fusion zone in as-weld state and after PWHT,

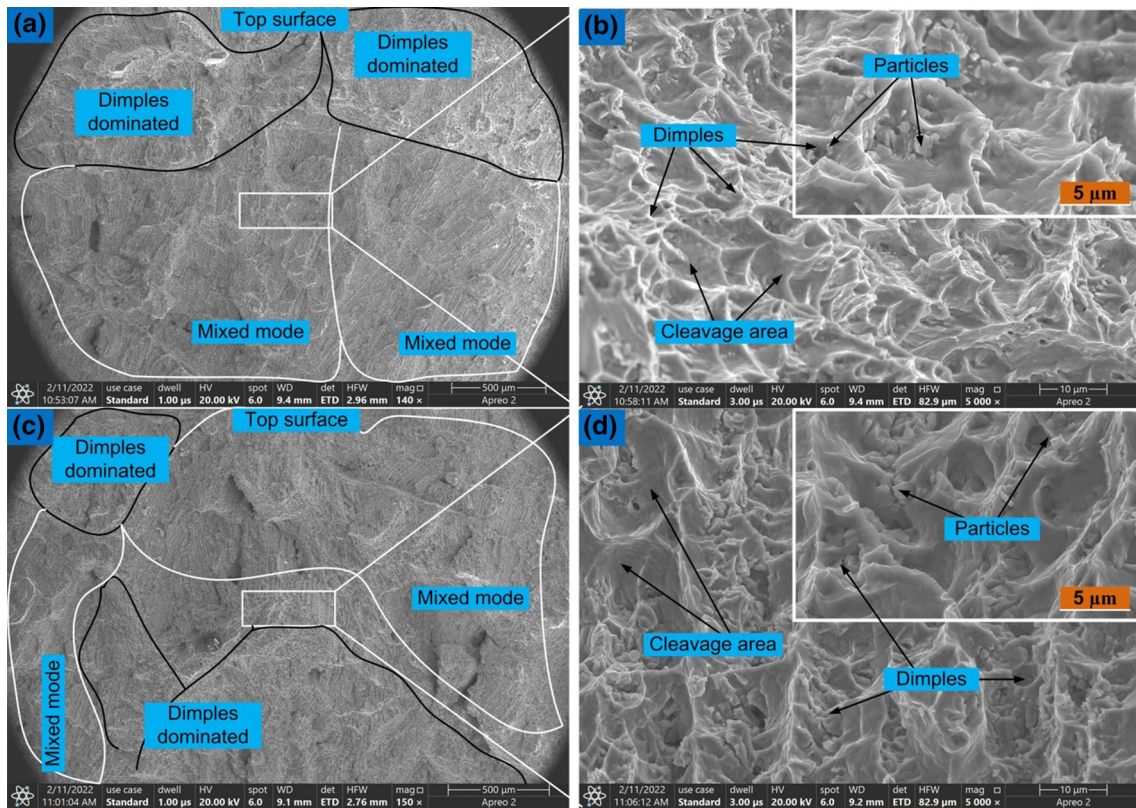
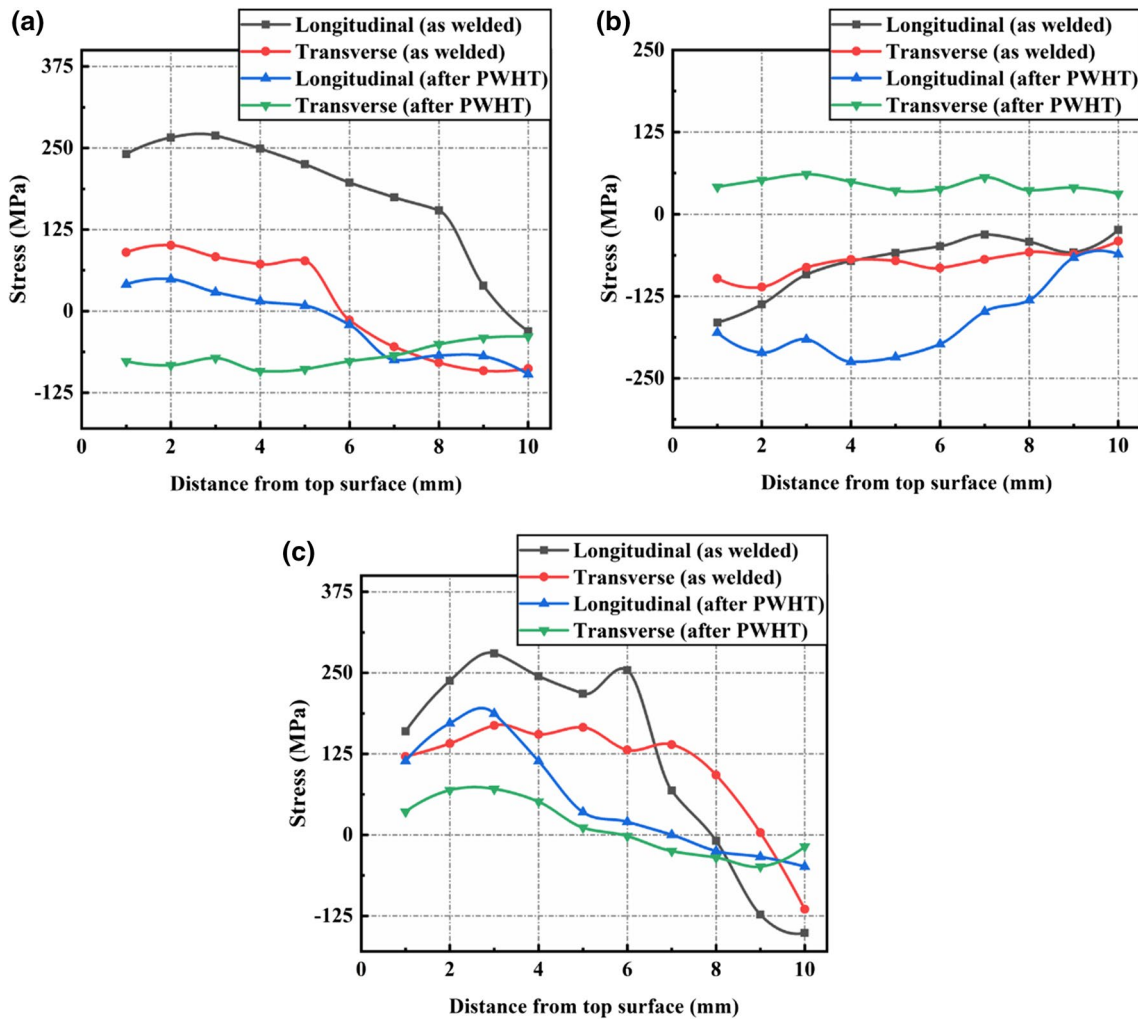


Fig. 29 Fractograph of the weld fusion zone of P92/304L SS DWJs (a, b) as-weld Charpy test specimen and (c, d) PWHT Charpy specimen



**Fig. 30** Residual stress profile for the **a** ERNiCrMo-3 weld zone, **b** P92 HAZ, **c** 304L SS HAZ, in as-weld situation and after PWHT

**Table 7** Residual stress data for 304L SS HAZ

Thickness (mm)	As-welded		After PWHT	
	Longitudinal (MPa)	Transverse (MPa)	Longitudinal (MPa)	Transverse (MPa)
1	160	121	114	36
2	238	141	172	69
3	280	169	187	71
4	245	155	114	51
5	218	166	35	11
6	254	131	20	-2
7	69	139	0	-25
8	-9	92	-25	-35
9	-124	3	-34	-49
10	-152	-115	-49	-18

respectively. The obtained Charpy impact test result satisfied the minimum required impact energy criteria.

(6) From the residual stress analysis of the weld zone, P92 HAZ, and 304L SS HAZ in the as-weld and PWHT condition, it was found that the maximum tensile longitudinal (280 MPa) and transverse (169 MPa) residual stresses were present at 304L SS HAZ in the as-weld condition. Also, after PWHT, the maximum tensile longitudinal and transverse residual stresses were observed at 304L SS HAZ. The PWHT is necessary for P92-304L SS DWJ to obtain the desired microstructure, improve the mechanical property, and mitigate the residual stresses.

**Acknowledgements** The authors would like to express sincere gratitude to “Science and Education Research Board” (SERB-India) for financial support of the project entitled “Mitigation of weldability

issues and residual stresses in dissimilar welded joints of ultra-supercritical power plants” under grant No: SRG/2019/001879.

## Declarations

**Conflict of interest** Author(s) have no conflict of interest.

**Ethical statements** The manuscript is original and not submitted elsewhere for publication.

## References

- Ritchie H, Roser M, Rosado P. Energy. In: Our World Data. 2020. <https://ourworldindata.org/energy>. Accessed 13 Oct 2022.
- Campbell RJ (2015) Increasing the efficiency of existing coal-fired power plants. *Coal-Fired Power Plants. Eff Improv Opt*, pp 77–111
- Di Gianfrancesco A. The fossil fuel power plants technology. Elsevier. 2017. <https://doi.org/10.1016/B978-0-08-100552-1.00001-4>.
- Viswanathan R, Henry JF, Tanzosh J, Stanko G, Shingledecker J, Vitalis B, Purgert R. U.S. Program on materials technology for ultra-supercritical coal power plants. *J Mater Eng Perform*. 2005;14:281–92. <https://doi.org/10.1361/10599490524039>.
- Lee J, Hwang J, Bae D. Welding residual stress analysis and fatigue strength assessment at elevated temperature for multi-pass dissimilar material weld between alloy 617 and p92 steel. *Met Mater Int*. 2018;24:877–85. <https://doi.org/10.1007/s12540-018-0086-7>.
- Viswanathan R, Bakker W. Materials for ultrasupercritical coal power plants—boiler materials: part 1. *J Mater Eng Perform*. 2001;10:81–95.
- Pandey C. Mechanical and metallurgical characterization of dissimilar P92/SS304 L welded joints under varying heat treatment regimes. *Metall Mater Trans A*. 2020;51:2126–42. <https://doi.org/10.1007/s11661-020-05660-0>.
- Kulkarni A, Dwivedi DK, Vasudevan M. Dissimilar metal welding of P91 steel-AISI 316L SS with Incoloy 800 and Inconel 600 interlayers by using activated TIG welding process and its effect on the microstructure and mechanical properties. *J Mater Process Technol*. 2019;274: 116280. <https://doi.org/10.1016/j.jmatprotec.2019.116280>.
- Sun Z. Feasibility of producing ferritic/austenitic dissimilar metal joints by high energy density laser beam process. *Int J Press Vessel Pip*. 1996;68:153–60. [https://doi.org/10.1016/0308-0161\(94\)00048-4](https://doi.org/10.1016/0308-0161(94)00048-4).
- Cao J, Gong Y, Zhu K, Yang Z, Luo X, Gu F. Microstructure and mechanical properties of dissimilar materials joints between T92 martensitic and S304H austenitic steels. *Mater Des*. 2011;32:2763–70. <https://doi.org/10.1016/j.matdes.2011.01.008>.
- Banovic SW, DuPont JN, Marder AR. Dilution and microsegregation in dissimilar metal welds between super austenitic stainless steel and nickel base alloys. *Sci Technol Weld Join*. 2002;7:374–83. <https://doi.org/10.1179/136217102225006804>.
- Sauraw A, Sharma AK, Fydrych D, Sirohi S, Gupta A, Świerczyńska A, Pandey C, Rogalski G. Study on Microstructural characterization, mechanical properties and residual stress of GTAW dissimilar joints of P91 and P22 steels. *Materials (Basel)*. 2021;14:6591. <https://doi.org/10.3390/ma14216591>.
- Kumar A, Pandey C. Development and evaluation of dissimilar gas tungsten arc-welded joint of P92 Steel/inconel 617 Alloy for advanced ultra-supercritical boiler applications. *Metall Mater Trans A*. 2022;53:3245–73. <https://doi.org/10.1007/s11661-022-06723-0>.
- Xu WH, Lin SB, Fan CL, Yang CL. Prediction and optimization of weld bead geometry in oscillating arc narrow gap all-position GMA welding. *Int J Adv Manuf Technol*. 2015;79:183–96. <https://doi.org/10.1007/s00170-015-6818-7>.
- Feng J, Guo W, Irvine N, Li L. Understanding and elimination of process defects in narrow gap multi-pass fiber laser welding of ferritic steel sheets of 30 mm thickness. *Int J Adv Manuf Technol*. 2017;88:1821–30. <https://doi.org/10.1007/s00170-016-8929-1>.
- Jula M, Dehmolaie R, Alavi Zaree SR. The comparative evaluation of AISI 316/A387-Gr91 steels dissimilar weld metal produced by CCGTAW and PCGTAW processes. *J Manuf Process*. 2018;36:272–80. <https://doi.org/10.1016/j.jmapro.2018.10.032>.
- Bhanu V, Gupta A, Pandey C. Role of A-TIG process in joining of martensitic and austenitic steels for ultra-supercritical power plants—a state of the art review. *Nucl Eng Technol*. 2022;54:2755–70. <https://doi.org/10.1016/j.net.2022.03.003>.
- Shuo W, Limin W, Yi C, Shuping T. Post-weld heat treatment and groove angles affect the mechanical properties of T92/super 304H dissimilar steel weld joints. *High Temp Mater Process*. 2018;37:649–54. <https://doi.org/10.1515/htmp-2016-0261>.
- Li S, Ren S, Zhang Y, Deng D, Murakawa H. Numerical investigation of formation mechanism of welding residual stress in P92 steel multi-pass joints. *J Mater Process Technol*. 2017;244:240–52. <https://doi.org/10.1016/j.jmatprotec.2017.01.033>.
- Shah Hosseini H, Shamanian M, Kermanpur A. Characterization of microstructures and mechanical properties of Inconel 617/310 stainless steel dissimilar welds. *Mater Charact*. 2011;62:425–31. <https://doi.org/10.1016/j.matchar.2011.02.003>.
- Nivas R, Singh PK, Das G, Das SK, Kumar S, Mahato B, Sivaprasad K, Ghosh M. A comparative study on microstructure and mechanical properties near interface for dissimilar materials during conventional V-groove and narrow gap welding. *J Manuf Process*. 2017;25:274–83. <https://doi.org/10.1016/j.jmapro.2016.12.004>.
- Shu F, Lv Y, Liu Y, Xu F, Sun Z, He P, Xu B. Residual stress modeling of narrow gap welded joint of aluminum alloy by cold metal transferring procedure. *Constr Build Mater*. 2014;54:224–35. <https://doi.org/10.1016/j.conbuildmat.2013.12.056>.
- Taraphdar PK, Mahapatra MM, Pradhan AK, Singh PK, Sharma K, Kumar S. Effects of groove configuration and buttering layer on the through-thickness residual stress distribution in dissimilar welds. *Int J Press Vessel Pip*. 2021;192: 104392. <https://doi.org/10.1016/j.ijpvp.2021.104392>.
- Saini N, Mulik RS, Mahapatra MM, Sharma NK, Li L. Dissolution of laves phase by re-austenitization and tempering of creep strength enhanced ferritic steel. *Mater Sci Technol (United Kingdom)*. 2020;36:631–44. <https://doi.org/10.1080/02670836.2020.1724404>.
- Mohyla P, Republic C. Influence of delta ferrite on mechanical and creep. (n.d.) 75–83.
- Fu JW, Yang YS, Guo JJ. Formation of a blocky ferrite in Fe-Cr-Ni alloy during directional solidification. *J Cryst Growth*. 2009;311:3661–6. <https://doi.org/10.1016/j.jcrysgro.2009.05.007>.
- Xu H, Xu MJ, Yu C, Lu H, Wei X, Chen JM, Xu JJ. Effect of the microstructure in unmixed zone on corrosion behavior of 439 tube/308L tube-sheet welding joint. *J Mater Process Technol*. 2017;240:162–7. <https://doi.org/10.1016/j.jmatprotec.2016.09.017>.
- Gabrel J, Bendick W, Vandenberghe B, Lefebvre B. Status of development of VM 12 steel for tubular applications in advanced power plants. *Energy Mater*. 2006;1:218–22. <https://doi.org/10.1179/174892406X173657>.
- Siefert JA, David SA. Weldability and weld performance of candidate austenitic alloys for advanced ultrasupercritical fossil power plants. *Sci Technol Weld Join*. 2014;19:271–94. <https://doi.org/10.1179/1362171814Y.0000000197>



30. Brózda J. New generation creep-resistant steels, their weldability and properties of welded joints: T/P92 steel. *Weld Int.* 2005;19:5–13. <https://doi.org/10.1533/wint.2005.3370>.
31. Taraphdar PK, Mahapatra MM, Pradhan AK, Singh PK, Sharma K, Kumar S. Measurement of through-thickness residual stresses under restrained condition in pressure vessel steel weld. In: Saran VH, Misra RK, editors. *Advances in systems engineering, Lecture notes in mechanical engineering*. Singapore: Springer; 2021. p. 119–25. [https://doi.org/10.1007/978-981-15-8025-3\\_13](https://doi.org/10.1007/978-981-15-8025-3_13).
32. Taraphdar PK, Kumar R, Pandey C, Mahapatra MM. Significance of finite element models and solid-state phase transformation on the evaluation of weld induced residual stresses. *Met Mater Int.* 2021. <https://doi.org/10.1007/s12540-020-00921-4>.
33. Guo X, Gong J, Jiang Y, Rong D. The influence of long-term aging on microstructures and static mechanical properties of P92 steel at room temperature. *Mater Sci Eng A.* 2013;564:199–205. <https://doi.org/10.1016/j.msea.2012.10.024>.
34. Chen G, Zhang Q, Liu J, Wang J, Yu X, Hua J, Bai X, Zhang T, Zhang J, Tang W. Microstructures and mechanical properties of T92/Super304H dissimilar steel weld joints after high-temperature ageing. *Mater Des.* 2013;44:469–75. <https://doi.org/10.1016/j.matdes.2012.08.022>.
35. Seo W-G, Suh J-Y, Singh A, Shim J-H, Lee H, Yoo K, Choi S-H. Microstructural evolution of P92 steel in IN740H/P92 dissimilar weld joints during creep deformation. *Mater Sci Eng A.* 2021;821:141614. <https://doi.org/10.1016/j.msea.2021.141614>.
36. Barbadikar DR, Sakthivel T, Ballal AR, Peshwe DR, Rao PS, Mathew MD, Barbadikar DR, Sakthivel T, Ballal AR, Peshwe DR, Syamala P. Materials at High Temperatures An assessment of mechanical properties of P92 steel weld joint and simulated heat affected zones by ball indentation technique. *Mater High Temp.* 2017;3409:1–11. <https://doi.org/10.1080/09603409.2017.1371913>.
37. Obiko J, Chown LH, Whitefield DJ. Microstructure characterisation and microhardness of P92 steel heat treated at the transformation temperatures. *IOP Conf Ser Mater Sci Eng.* 2019. <https://doi.org/10.1088/1757-899X/655/1/012014>.
38. Maddi L, Ballal AR, Peshwe DR, Mathew MD. Influence of normalizing and tempering temperatures on the creep properties of P92 steel. *High Temp Mater Process.* 2020;39:178–88. <https://doi.org/10.1515/htmp-2020-0033>.
39. Wang Y, Li L, Kannan R. Transition from Type IV to Type I cracking in heat-treated grade 91 steel weldments. *Mater Sci Eng A.* 2018;714:1–13. <https://doi.org/10.1016/j.msea.2017.12.088>.
40. Kou S, Yang YK. Fusion-boundary macrosegregation in dissimilar-filler welds. *Weld J (Miami Fla).* 2007;86:303–12.
41. Cieslak MJ, Headley TJ, Kollie T, Romig AD. Melting and solidification study of Alloy 625. *Metall Trans A Phys Metall Mater Sci.* 1988;19A:2319–31. <https://doi.org/10.1007/BF02645056>.
42. Silva CC, De Miranda HC, Motta MF, Farias JP, Afonso CRM, Ramirez AJ. New insight on the solidification path of an alloy 625 weld overlay. *J Mater Res Technol.* 2013;2:228–37. <https://doi.org/10.1016/j.jmrt.2013.02.008>.
43. Dak G, Pandey C. A critical review on dissimilar welds joint between martensitic and austenitic steel for power plant application. *J Manuf Process.* 2020;58:377–406. <https://doi.org/10.1016/j.jmapro.2020.08.019>.
44. Ramkumar KD, Abraham WS, Viyash V, Arivazhagan N, Rabel AM. Investigations on the microstructure, tensile strength and high temperature corrosion behaviour of Inconel 625 and Inconel 718 dissimilar joints. *J Manuf Process.* 2017;25:306–22. <https://doi.org/10.1016/j.jmapro.2016.12.018>.
45. Deng D, Murakawa H. Numerical simulation of temperature field and residual stress in multi-pass welds in stainless steel pipe and comparison with experimental measurements. *Comput Mater Sci.* 2006;37:269–77. <https://doi.org/10.1016/j.commatsci.2005.07.007>.
46. Li S, Hu L, Dai P, Bi T, Deng D. Influence of the groove shape on welding residual stresses in P92/SUS304 dissimilar metal butt-welded joints. *J Manuf Process.* 2021;66:376–86. <https://doi.org/10.1016/j.jmapro.2021.04.030>.
47. Venkata KA, Kumar S, Dey HC, Smith DJ, Bouchard PJ, Truman CE. Study on the effect of post weld heat treatment parameters on the relaxation of welding residual stresses in electron beam welded P91 steel plates. *Proc Eng.* 2014;86:223–33.
48. Deng D, Zhang Y, Li S, Tong Y. influence of solid-state phase transformation on residual stress in P92 steelwelded joint. *Jinshu Xuebao/Acta Metall Sin.* 2016;52:394–402. <https://doi.org/10.11900/0412.1961.2015.00371>.
49. Maduraimuthu V, Vasudevan M, Muthupandi V, Bhaduri AK. Effect of activated flux on the microstructure, mechanical properties, and residual stresses of modified 9Cr-1Mo steel weld joints. *Metall Mater Trans B.* 2012;43:123–32. <https://doi.org/10.1007/s11663-011-9568-4>.
50. David SA, Siefert JA, Feng Z. Welding and weldability of candidate ferritic alloys for future advanced ultrasupercritical fossil power plants. *Sci Technol Weld Join.* 2013;18:631–51. <https://doi.org/10.1179/1362171813Y.0000000152>.

**Publisher's Note** Springer Nature remains neutral with regard to jurisdictional claims in published maps and institutional affiliations.

Springer Nature or its licensor holds exclusive rights to this article under a publishing agreement with the author(s) or other rightsholder(s); author self-archiving of the accepted manuscript version of this article is solely governed by the terms of such publishing agreement and applicable law.